SEDIMENTOLOGY the journal of the International Association of Sedimentologists

Sedimentology (2013) **60**, 911–934 doi: 10.1111/j.1365-3091.2012.01370.x

Varved sediments of Lake Yoa (Ounianga Kebir, Chad) reveal progressive drying of the Sahara during the last 6100 years

PIERRE FRANCUS*,†, HANS VON SUCHODOLETZ‡,§, MICHAEL DIETZE§, REIK V. DONNER¶, FRÉDÉRIC BOUCHARD*, ANN-JULIE ROY**, MAUREEN FAGOT††, DIRK VERSCHUREN††,[1] and STEFAN KRÖPELIN‡‡,[1]

**Institut National de la Recherche Scientifique, Centre Eau, Terre et Environnement, Québec, QC, G1K 9A9, Canada (E-mail: pfrancus@ete.inrs.ca)*

†GEOTOP Research Center, Montréal, QC, H3C 3P8, Canada

‡Institute of Geography, University of Leipzig, D-04103, Leipzig, Germany

§Institute of Geography, Dresden University of Technology, D-01069, Dresden, Germany

¶Potsdam Institute for Climate Impact Research, D-14473, Potsdam, Germany

***Département de Géographie, Centre d'étude nordique, Québec, QC, G1V 0A6, Canada*

††Limnology Unit, Department of Biology, Ghent University, B-9000, Gent, Belgium

‡‡Institute of Prehistoric Archaeology, University of Cologne, D-50823, Köln, Germany

Associate Editor – Daniel Ariztegui

ABSTRACT

The sedimentological and geochemical properties of a 7·47 m long laminated sequence from hypersaline Lake Yoa in northern Chad have been investigated, representing a unique, continuous 6100 year long continental record of climate and environmental change in the eastern Central Sahara. These data were used to reconstruct the Mid to Late Holocene history of this currently hyper-arid region, in order to address the question of whether the Mid Holocene environmental transition from a humid to a dry Sahara was progressive or abrupt. This study involved a suite of analyses, including petrographic and scanning electron microscope examination of thin sections, X-ray diffraction, X-radiography, granulometry, loss on ignition and magnetic susceptibility. The potential of micro-X-ray fluorescence core scanning was tested at very high resolution. Detailed microscopic investigation revealed the sedimentary processes responsible for the formation of the fine laminations, identified the season during which they were formed, and confirmed their annually rhythmic nature. High-resolution X-ray fluorescence core scanning allowed the distinction of each individual lamination over the entire record, opening new perspectives for the study of finely laminated sediment sequences. Geochemical and mineralogical data reveal that, due to decreasing monsoon rainfall combined with continuous and strong evaporation, the hydrologically open and fresh Mid Holocene Lake Yoa slowly evolved into the present-day hypersaline brine depleted in calcium, which has existed for about the past 1050 years. During the oldest part of the investigated period, Lake Yoa probably contained a permanently stratified lower water column that was nevertheless disrupted relatively frequently by mixing events. Deep-water anoxia became more stable because of increased salinity-driven density stratification. In parallel, the sediment grain-size proxies record a progressive increase of aeolian input in the course of the last 6100 years. Altogether, all geochemical and sedimentological indicators point to a progressive drying of the eastern Central Sahara, strengthening previous conclusions based on palaeoecological indicators.

[1]These authors contributed equally to this study.

Keywords Aeolian input, brine evolution, grain size, magnetic susceptibility, palaeoredox, X-ray fluorescence core scanning.

INTRODUCTION

Lake Yoa in the Ounianga region of northern Chad is very likely to contain the only continuous lake-sediment record of the Holocene environmental history of the eastern Central Sahara (Kröpelin, 2007). Unlike other records from arid North Africa (reviewed by Hoelzmann *et al.*, 2004), this unique archive has been preserved from desiccation, and hence from erosion by wind deflation, because Lake Yoa has enjoyed substantial ground-water input throughout the Holocene and until the present. The sediment record of Lake Yoa is also unique because (at least) the upper 7·47 m of the sequence, which covers the last 6100 years, is comprised completely of millimetre-scale laminations that are interpreted as annual deposits, that is, varves (Kröpelin *et al.*, 2008). From this unique palaeoenvironmental archive, Kröpelin *et al.* (2008) produced parallel multi-proxy reconstructions of the Mid and Late Holocene evolution of both the terrestrial ecosystem in the Ounianga region and the aquatic ecosystem of Lake Yoa. This highly resolved sequence revealed a gradual Mid Holocene desiccation of the terrestrial ecosystem in the eastern Central Sahara (Kröpelin *et al.*, 2008), contradicting the abrupt climate and vegetation change *ca* 5500 years ago inferred from a record of Saharan dust deposition in marine sediments off the Mauritania coast (deMenocal *et al.*, 2000). Eggermont *et al.* (2008) described the past zoobenthos and zooplankton communities of Lake Yoa, and detailed the transfer-function method used to reconstruct past salinity changes on the basis of fossil chironomid assemblages. This proxy, and a parallel reconstruction based on fossil-diatom assemblages, both indicated that Lake Yoa switched rather quickly from a fresh to a saline lake between 4200 and 3800 years ago, associated with its transition from an open to closed hydrological system (Kröpelin *et al.*, 2008). In contrast, the regional vegetation history inferred from the pollen record of Lake Yoa (Kröpelin *et al.*, 2008), and detailed further by Lézine (2009) and Lézine *et al.* (2011), showed a more progressive decrease of tropical tree species between *ca* 5600 and 4300 years ago, and further gradual desiccation of the landscape until the desert environment of today was formed 2700 years ago.

In this study, the focus is on multi-proxy sedimentological, mineralogical and geochemical analyses of the Lake Yoa sediment record which aims to: (i) provide the sedimentological context for the deposition and preservation of biological indicators used for reconstructing the aquatic and terrestrial ecosystems; (ii) understand the processes responsible for the accumulation and preservation of the fine sediment laminations, and to confirm their annual nature; and (iii) produce palaeoenvironmental reconstructions of the local aquatic and surrounding terrestrial ecosystems complementary to those based on the biological indicators previously published.

STUDY AREA

Lake Yoa [19·03°N, 20·31°E., 380 m above sea-level (a.s.l.)] is currently hypersaline (68 mS cm^{-1}) and has a surface area of 4·3 km^2 (Fig. 1). Its bathymetry is characterized by a rather flat central lake floor with a depth of 24 to 26 m, a gently sloping bottom towards the south-east, and a more steeply sloping bottom in all other directions because of encroaching sand dunes. The lake is part of a cluster of lacustrine bodies (Ounianga Kebir) that occupy a depression between the Tibesti and Ennedi mountains (Fig. 1B). The Ounianga lakes are fed by fresh fossil ground-water located in the Nubian Sandstone Aquifer System (Thorweihe, 1990), which was last recharged during the humid Early Holocene (International Atomic Energy Agency, 2007).

The subtropical hyper-arid climate of this area is characterized by high daytime temperatures, cool nights, negligible rainfall and dry north-easterly trade winds year round (Kröpelin *et al.*, 2008). Mean monthly day and night-time temperatures range from 26˚C and 15˚C in winter (December through to January) to 42˚C and 26˚C, respectively, in summer (June to July). This strong seasonal temperature gradient is also clear from reanalysis by the National Center for Environmental Prediction (NCEP) and the

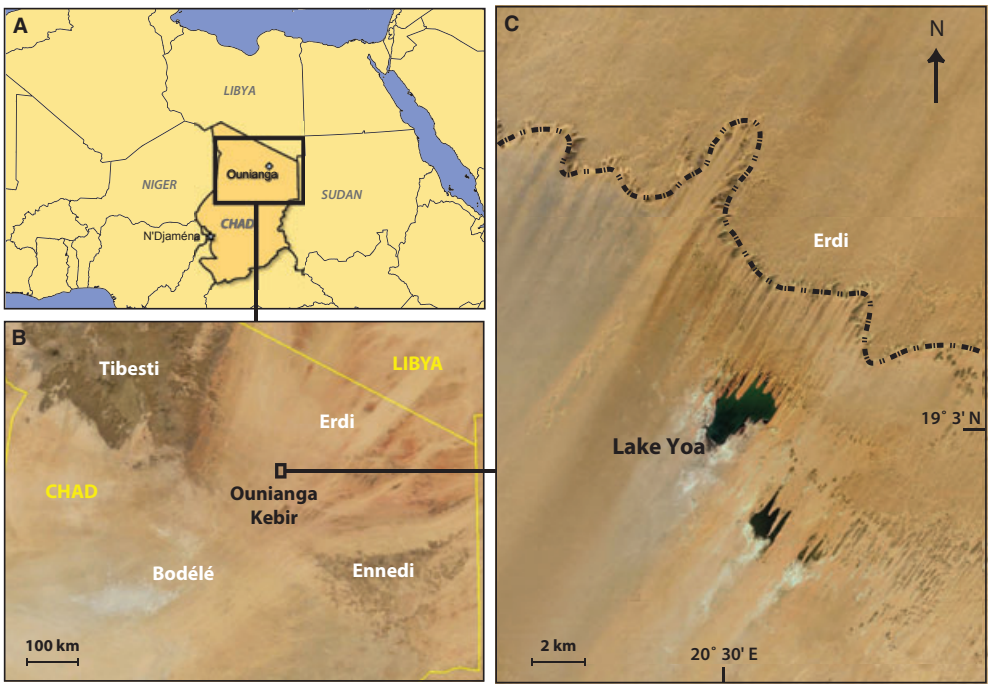

Fig. 1. Location map: (A) general location; (B) location of Ounianga Kebir with respect to the Tibesti and Ennedi Mountains and the downwind Bodélé depression; (C) location of Lake Yoa and other hypersaline lakes in Ounianga Kebir, in relation to the nearby escarpment (dashed lines) and dunes encroaching from the north-east. Source: Google Earth, accessed on 15 June, 2011.

National Center for Atmospheric Research (NCAR) of surface-level data for the 2·5° grid cell centred on Ounianga Kebir (Table 1). Near-surface speeds of the persistent north-easterly winds at Faya Largeau and in the downwind Bodélé depression (Washington *et al.*, 2006) also display an annual cycle with a maximum in the winter months and a minimum between July and September. The number of large dust plumes over the Bodélé depression reaches a maximum from December to April (Washington *et al.*, 2006). These harmattan-related dust storms are thought to be due to pressure surges after outbreaks of cold air from the mid-latitudes between October and April (Goudie & Middleton, 2001). Annual rainfall is erratic, ranging from 0 to 21 mm between 1953 and 1967 (mean 3·9 mm), and is of southerly (monsoonal) origin occurring during summer. Mean annual evaporation is >6000 mm (Kröpelin *et al.*, 2008). The level of Lake Yoa fluctuates seasonally about one metre between a minimum in September or October and maximum in March or April (Capot-Rey, 1961).

Table 1. Monthly average temperature according to the NCEP/NCAR reanalysis data set for surface level using the 2·5° grid cell centred on Ounianga Kebir.

Average Temperature	
Month	1970 to 2010
Jan	14·40
Feb	17·15
Mar	21·28
Apr	26·47
May	29·41
Jun	30·29
Jul	30·30
Aug	30·24
Sep	28·14
Oct	24·30
Nov	18·52
Dec	15·15
Annual	23·82

MATERIAL AND METHODS

Core acquisition

In 2003 and 2004, overlapping cores were recovered in 24·3 m water depth using a Uwitec gravity corer (Uwitec, Mondsee, Austria), a single-drive piston corer (Wright, 1980) and a square-rod piston corer (Wright, 1967) deployed from an anchored platform; the deepest core sections were recovered using rigid aluminium

casing to support the push rods. The cores were transported either by capping and taping the transparent polycarbonate tubes used for recovery, or extruded in the field and packed in a transparent PVC sheet supported by PVC water pipe cut lengthwise into two halves. Archive halves were initially shipped to the US National Core Repository (LacCore) facility at the University of Minnesota for non-destructive core-scanning analyses, and working halves were shipped to Ghent University for exploratory sedimentological analyses and extraction of plant macrofossils for radiocarbon dating.

Laboratory work

Core logging and scanning

Cores were photographed at the LacCore facility of the University of Minnesota, using a DMT CoreScan digital line-scan camera with a pixel size of 50 μm (DMT GmbH, Essen, Germany). Volume-specific magnetic susceptibility (κ) was measured at 5 mm intervals with a MS2E point sensor (Bartington Instruments Ltd, Witney, UK) installed on a Multisensor Core Logger (Geotek Ltd, Daventry, Northants, UK). Magnetic susceptibility profiles of the overlapping core sections allowed construction of a 7·47 m long composite sequence, with fine-tuning of the cross-matches using fine sediment laminations as visual marker horizons. Water content, porosity, organic and carbonate content were measured at Ghent University on the working halves, using loss on ignition (LOI) methods (Bengtsson & Enell, 1986) on fixed volumes of 1·00 ml wet mud in continuous 1 cm intervals throughout the sequence. In core sections where extraction of exact volumetric sub-samples was difficult, porosity was estimated based on a regression of porosity against water content obtained from the rest of the sequence. Water content, organic and carbonate content data were used to calculate mass-specific magnetic susceptibility (χ) at 1 cm intervals. Assuming that the diamagnetic material of organic matter and carbonate minerals contribute little to total magnetic susceptibility (Evans & Heller, 2003), magnetic susceptibility was normalized against the dry mass of the samples excluding these two components, as in Kröpelin *et al.* (2008). These derived χ values thus only represent the detrital mineral fraction of the sediment, plus a mostly low (but not measured at intervals of 1 cm) quantity of diatom silica. This solid-phase biogenic silica (BSi) in Lake Yoa sediments (data presented by Kröpelin *et al.*, 2008) was measured by digesting sediment samples in 1% Na_2CO_3 for set periods of up to 3 h at 85°C in a heated shaking bath. Sequential sub-samples were neutralized with HCl, and the dissolved silica was measured by spectrophotometry (Conley & Schelske, 2001). Note that in the present paper, the definitions of Last (2001) are used to describe three important sediment components: detrital material is the inorganic component brought into the lake from external sources through both fluvial and aeolian transport, endogenic minerals are minerals that originate from the water column by chemical precipitation, and authigenic minerals are formed by diagenetic transformation occurring after sedimentation. Furthermore, a sediment layer refers to any tabular body of mud with no thickness limitation, whereas a lamina designates layers thinner than 1 cm (Jackson, 1997). The sedimentary facies classification scheme, as well as the definition of sediment layering, follows Schnurrenberger *et al.* (2003).

The archive core halves were measured with an Itrax microfluorescence (μ-XRF) core scanner (Cox Analytical Systems, Molndal, Sweden) at the Institut National de la Recherche Scientifique in Quebec City. Prior to measurement, the cores were photographed again, using the Itrax digital camera with a pixel size of 100 μm. Furthermore, 16-bit X-radiographs were acquired with similar resolution. Comparison of these core images with the photographs originally taken in Minnesota revealed that portions of the five upper core sections had suffered from compaction during transport to Quebec. This compaction was 2·13% on average but not linear nor uniform within and between cores (Table 2). To ensure correct comparison of the Itrax data with those generated in Ghent and elsewhere, 215 marker beds were precisely located at an average interval of 2·2 cm on both sets of images. Subsequently, the thickness of each interval in the archive halves (i.e. the Itrax data) was corrected to match the original master composite depth scale, allowing direct comparison of all proxy data. As a warning for all multi-proxy analyses made on soft sediment sequences, this differential compaction during courier shipping was detected (and could be corrected) only because of the finely laminated nature of the Lake Yoa sediment. The Itrax data comprise 73 210 μ-XRF spectra measured at 100 μm resolution, with acquisition conditions of 30 kV, 30 mA and 5 sec of integration time. To adjust for instrumental bias and matrix effect (Croudace *et al.*,

Table 2. Compaction of core sections after courier-shipping from Minnesota to Québec, as inferred from digital images examined before (Gent) and after (Québec).

	GENT (cm)			QUÉBEC (cm)			Difference	
							Gent	Québec
Core section	Section From–To	Composite From–To	Total length	Section From–To	Composite From–To	Total length	cm	%
OUNIK03-3G	17–79	0–62	62·0	22·2–81·8	0–59·6	59·6	2·4	3·87
OUNIK03-2Pla	42–99·4	62–119	57·0	40·5–90·4	59·6–109·5	49·9	7·1	12·46
OUNIK03-2Plb	0–89	119–208	89·0	0–85	109·5–194·5	85·0	4·0	4·49
OUNIK03-2PII	22–103·5	208–289·5	81·5	22·8–103·6	194·5–275·3	80·8	0·7	0·86
OUNIK 03-2PIII	20–94	289·5–363·3	73·8	21·3–93·8	275·3–347·7	72·4	1·4	1·90
OUNIK 04-1PI	75–100·1	363·3–388·7	25·4	74·6–100	347·7–373·1	25·4	0·0	0·00
OUNIK 04-1PII	5·2–102·3	388·7–486·2	97·5	2·5–100	373·1–470·6	97·5	0·0	0·00
OUNIK 04-1PIII	4·5–108·8	486·2–588·9	102·7	3·5–106·1	470·6–573·2	102·6	0·1	0·10
OUNIK 04-1PIV	6–101·4	588·9–684	95·1	4·8–99·8	573·2–668·2	95·0	0·1	0·11
OUNIK04-1PV	14–77·7	684–747·1	63·1	12·7–75·7	668·2–731·2	63·0	0·1	0·16
TOTAL			747·1			731·2	15·9	2·13

2006), results are expressed as element/kcps (kcps = total counts per spectrum, in thousands) or as element ratios. From the μ-XRF data, inc/coh (incoherent/coherent or Compton/Raleigh scattering) was calculated, which relates inversely to mean atomic number. This ratio varies with sediment packing, water and organic carbon content (Croudace *et al.*, 2006).

Destructive sedimentological analyses

Samples for grain-size analysis presented in this study were extracted from contiguous 2 cm intervals and prepared as follows: about 3 g of wet mud were placed into a vessel and treated with 10% and 30% HCl to destroy calcium carbonate. After rinsing with de-ionized water, H_2O_2 (30%) was added to destroy any organic material present. To accelerate this reaction, samples were heated for several hours at 65°C in a water bath, and H_2O_2 was added continuously. To ensure that all organic material was destroyed, samples were left for another week in H_2O_2 at room temperature, before rinsing with de-ionized water. Then, 40 ml of 2M $NaCO_3$ were added to remove biogenic silica; the samples were placed in a water bath (90°C) for 6 h and shaken every hour. Subsequently, smear-slides of every sample were checked for remaining diatoms using a microscope. If diatoms were still present, the sample was treated again with $NaCO_3$ for another 2 h. Finally, 6 ml of 0·05 M $(NaPO_3)_6$ $Na_2P_4O_7$ were added and the sample was sonicated for 30 minutes to disperse the clays. Grain-size measurements were carried out using an LS 13 320 laser particle counter (Beckman Coulter Inc., Brea, CA, USA) at the Large Lakes Observatory of the University of Minnesota; reported values are the average of three measurements on each sample. The clay/silt limit of 7·4 μm for this instrument was determined using five test samples. The grain-size distribution of these samples had been determined on the basis of Stoke's law using a Koehn apparatus at the University of Bayreuth. This limit is in accordance with the results of Konert & Vandenberghe (1997).

The fine sand (75 to 150 μm) fraction was also determined independently at Ghent University by weighing the residue of wet-sieved sub-samples after burning at 1000°C, similarly from contiguous 2 cm intervals. These are the fine sand data presented in Kröpelin *et al.* (2008); values of fine sand content (as a percentage of the total mineral sediment fraction) from the laser and gravimetric data are highly correlated ($R^2 = 0{\cdot}90$).

The grain-size distributions were characterized using the *W*-ratio, a new statistical parameter derived from the *U*-ratio of Vandenberghe *et al.* (1993, 1997) as $W = (U - 1)/(U + 1)$; U is a traditional measure for the abundance ratio between two (coarse/fine) grain-size classes, in which the grain-size classes can be defined by the three zero crossings of the first two principal components derived from the full grain-size record (Donner, 2007). Unlike U, the W-ratio has the advantage of being normalized ($-1 \leq W \leq 1$), thus indicating dominance of fine clastic material when W is negative and dominance of coarse clastic material when W is positive.

The bulk mineralogy of the Lake Yoa sequence was determined qualitatively at nine discrete intervals using X-ray diffraction (XRD). For this purpose, 1 cm^3 samples were air-dried for several days, ground by hand and dry-sieved to a maximal grain size of 63 μm. Aliquots of 20 to 30 mg each were placed on plastic sample mounts as un-oriented powdered samples. Measurements were carried out at the Technical University of Dresden with an X-ray diffractometer D 5000 (Siemens AG, Munich, Germany) using the following settings: CoKα radiation, 40 kV, 30 mA, from 2° to 80° 2θ angle interval, 4 s step scan, 0·03° step size, aperture 20, 30 rpm of the sample desk. To investigate the clay mineral composition, 1 cm^3 samples from 32 other intervals were analysed. These samples were also air-dried and 10 mg were dispersed in de-ionized water to retrieve the fraction < 2 μm from Atterberg cylinders. After drying at 30°C, the sediment was again mixed with 10 cm^3 de-ionized water, poured onto glass slides and left to dry at room temperature, to allow the clay minerals to orientate. Each sample was measured three times after the following preparation steps: air drying, solvation with ethylene glycol (48 h) and heat treatment (2 h at 550°C). Measurements were carried out with the same XRD instrument as described above, but using from 2° to 36·5° 2θ angle interval, a step scan of 3 s and a step size of 0·01°. Interpretation followed standard procedures (Dixon & Weed, 1995; Moore & Reynolds, 1997).

Ten intervals representing all of the macroscopically distinct sedimentary facies along the composite sequence were sampled for thin sections using the technique outlined in Francus & Asikainen (2001). The 7 cm long undisturbed slabs were dehydrated by freeze-drying, and impregnated by Spurr's low viscosity resin under a low vacuum (Lamoureux, 1994). Subsequently, thin sections were prepared using standard techniques, and analysed at the Institut National de la Recherche Scientifique in Quebec City using a petrographic microscope and an EVO 50 Scanning Electron Microscope (SEM: Carl Zeiss NTS GmbH, Germany) in backscattered mode. Energy Dispersive Spectrometer (EDS) analyses and maps were performed using an INCA Energy (Oxford Instruments plc, Tubney Woods, UK) attached to the SEM.

Finally, the chemical composition of the full variety of facies present in the upper third of the sequence was determined at 13 discrete intervals, between 1 mm and 4 mm thick, through analysis of 16 major, minor and trace elements by inductively coupled plasma atomic emission spectrometry (ICP-AES) using a Vista AX CCO Simultaneous ICP-AES (Varian Inc., Palo Alto, CA, USA), at the Institut National de la Recherche Scientifique (Quebec City, Canada; Table 3).

RESULTS

Chronology and stratigraphy

The age model established by Kröpelin *et al.* (2008) was used; this is constrained by a total of 11 AMS ^{14}C dates on bulk organic matter calibrated using INTCAL04 (Reimer *et al.*, 2004) after subtracting the modern lake-carbon reservoir age from all bulk ^{14}C and *Typha* rhizome ages. This correction of 1467 ± 44 years is the mean ^{14}C age difference between two pairs of ^{14}C dates on terrestrial and bulk organic matter, and between the uppermost bulk ^{14}C date and the corresponding varve count, assuming continuous deposition. This age model is the second-order polynomial regression:

$$\begin{aligned}\text{Age}(\text{cal yr BP}) = &-13 + 6{\cdot}734(\text{depth} - 7) \\ &+ 0{\cdot}002023((\text{depth} - 7)^2)\end{aligned} \quad (1)$$

with depth in centimetres, and 7 cm the depth of the ^{137}Cs peak caused by sub-aerial nuclear bomb testing in 1963 to 1964 (Appleby, 2001); calibrated ages in the text and figures are rounded to the nearest 50 years. Counting the, on average, 1·6 mm thick couplets of light and dark lamination from the intact core surface to the ^{137}Cs peak confirmed the annual rhythm of the couplets. Preliminary lamination counts on the entire sequence are consistent with the ^{14}C-based age model within error range, corroborating the hypothesis that these lamination couplets are annual deposits, that is, varves.

The Lake Yoa sequence has been divided into six stratigraphic units (I to VI). The boundaries of these units coincide with the five successive time periods considered by Kröpelin *et al.* (2008), except that their uppermost zone has been divided further into two units (V and VI) to account for a major geochemical shift at 158 cm sediment depth. These units are listed in Table 4.

Table 3. Elemental concentrations using inductively coupled plasma atomic emission spectrometry (ICP-AES).

Sample depth (cm)	Total %	Al_2O_3 %	CaO %	Fe_2O_3T%	K_2O %	MgO %	MnO %	Na_2O %	P_2O_5 %	S %	SiO_2%	TiO_2 %	Sr p.p.m.	Zr p.p.m.
8·10	100·12	4·21	2·20	1·85	0·99	2·65	0·0275	2·78	0·0750	0·110	84·7	0·41	97	439
18·20	99·96	5·17	2·09	2·24	1·15	2·04	0·0285	3·49	0·0810	0·194	82·8	0·54	102	641
29·70	94·62	5·56	3·75	2·47	1·85	4·83	0·0510	5·27	0·106	0·171	70·0	0·47	157	405
31·80	99·37	2·46	0·38	1·05	0·45	0·36	0·0096	0·98	< 0·049	0·0565	93·3	0·26	33	356
43·15	97·59	2·72	0·67	1·23	0·58	0·95	0·0165	1·18	< 0·034	0·0541	89·8	0·32	41	338
44·35	99·52	5·06	2·24	2·31	1·31	2·91	0·0421	3·46	0·0740	0·143	81·4	0·44	102	371
122·70	97·98	6·33	2·23	2·71	1·45	2·10	0·0345	3·11	0·0750	0·190	79·0	0·62	108	703
152·50	97·33	5·48	3·00	2·43	1·51	2·92	0·0305	4·32	0·0820	0·187	76·7	0·53	128	663
160·45	96·70	3·93	25·70	1·64	0·71	2·45	0·0538	2·91	0·0860	0·640	57·9	0·38	787	418
166·75	99·34	4·95	17·60	2·02	1·19	3·10	0·0408	5·02	0·106	0·735	63·9	0·48	566	491
172·15	98·04	4·26	23·90	1·82	0·79	2·95	0·0465	3·11	0·0890	0·577	59·8	0·38	748	380
269·00	100·39	7·12	9·55	2·96	1·24	3·25	0·0458	2·75	0·0930	0·0976	72·4	0·65	338	740
269·15	99·76	7·22	10·60	3·26	1·15	3·65	0·0479	3·06	0·109	0·122	69·6	0·64	361	650

Characterization of sedimentary facies

The entire upper 7·47 m of the Lake Yoa sediment sequence consists of mostly finely laminated clayey to sandy mud. Notwithstanding its fairly uniform appearance throughout, the bulk sediment composition varies considerably with values of organic matter ranging from 5 to 20%, carbonate from 5 to 25% and diatom silica from 1 to 13%.

Lower Laminated Facies (Fig. 2)

This facies is present in units I to V. Macroscopically, the laminations consist of alternating light and dark brown layers (Fig. 2A). Under the petrographic microscope, three types of laminae are visible (Fig. 2B). The first type of lamina, macroscopically corresponding to the distinct light-brown coloured layer, is a micritic lamina (mic) with traces of detrital grains. Under SEM-EDS, this lamina is Ca-rich. Small carbonate rhombohedra are visible (Fig. 2C), together with very small siliciclastic silt grains rich in Fe. In the X-radiographs, these micritic laminae are dense and characterized by marked Ca/Ti peaks (Fig. 2E), enrichments in Sr/kcps, and relatively low values of Sr/Ca and Si/kcps. The second type of lamina, forming one part of the dark brown macroscopic layers, is composed of matrix-supported (i.e. grains are not touching each other; Tucker, 2001) and rounded very fine to medium sand, finer detrital material including mineral silt and clay, some organic matter and detrital carbonates. Chemical maps acquired using SEM-EDS confirm this structure: Si predominates in the rounded medium to very fine sand grains, whereas silt-sized grains are Fe-rich. Under the Itrax core scanner, these sandy laminae (mss) are characterized by high Si/kcps, Fe/kcps and Ti/kcps, whereas Ca/Ti is low (Fig. 2E). The third type of lamina, forming the other part of the dark brown layers, is mainly

Table 4. Composite core depths and ages of stratigraphic boundaries defined in this study.

	Depth (cm)		Age (ka cal BP)	
	Bottom	Top	Lower	Upper
Unit VI	158	0	1·05	−0·06
Unit V	370	158	2·70	1·05
Unit IV	512	370	3·90	2·70
Unit III	557	512	4·30	3·90
Unit II	697	557	5·60	4·30
Unit I	747	697	6·10	5·60

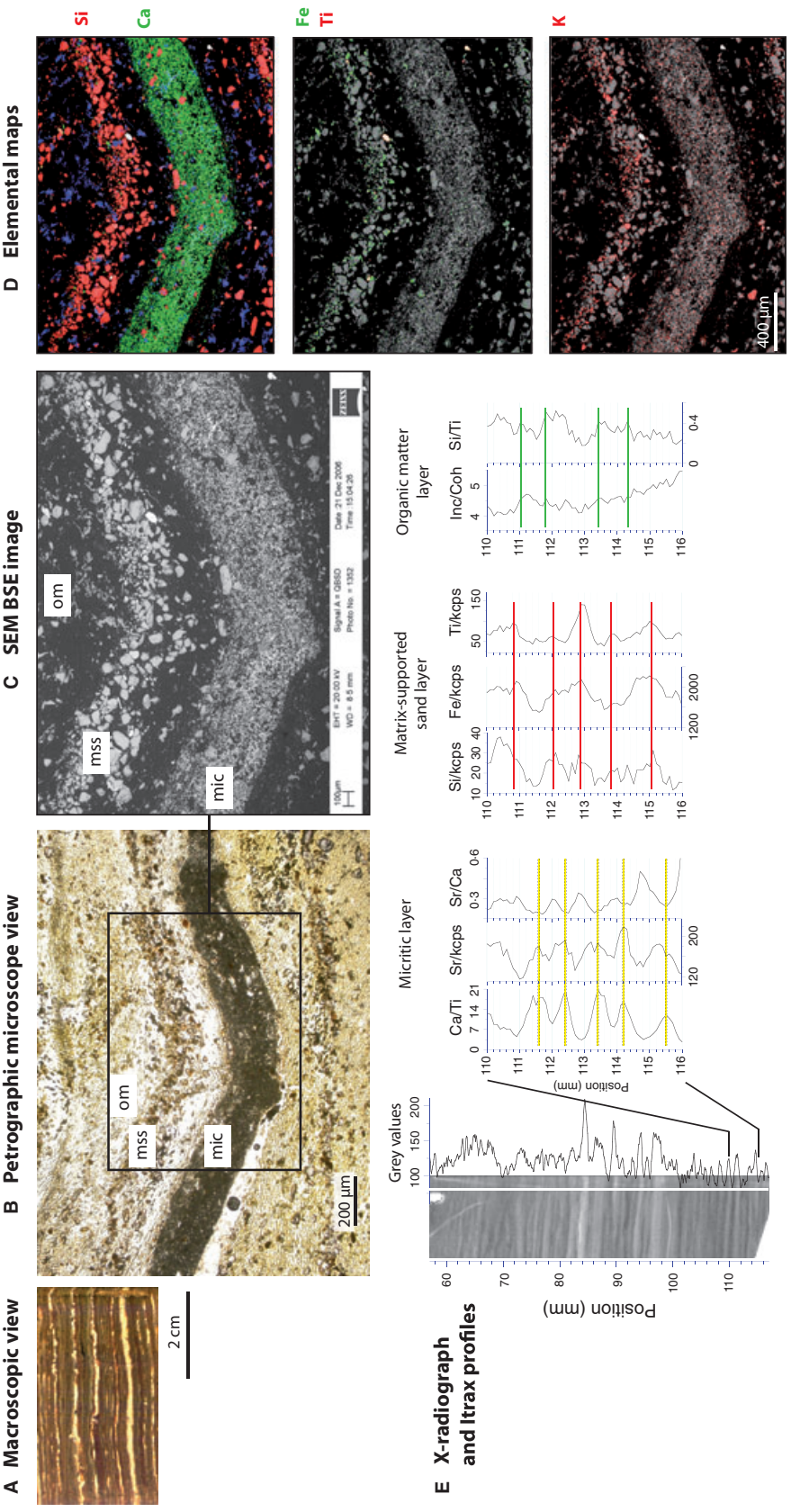

Fig. 2. Example of the Lower Laminated Facies. (A) View of the core surface. (B) Photomicrograph in plain light ('mic': micritic lamina; 'mss': matrix-supported sand lamina; 'om': organic-rich lamina). (C) SEM BSE image. (D) Elemental maps acquired using EDS. (E) Itrax measurements of selected chemical elements. From left to right: X-radiograph of a 6 cm long impregnated block used to make thin sections and its grey-scale profile along the white vertical line (denser sediments are darker); 6 mm thick close-up of selected geochemical profiles: yellow horizontal lines delineate examples of micritic laminae, red lines correspond to matrix-supported sand laminae and green lines correspond to organic-rich laminae. Depths are relative to the reference position of the sample in the instrument.

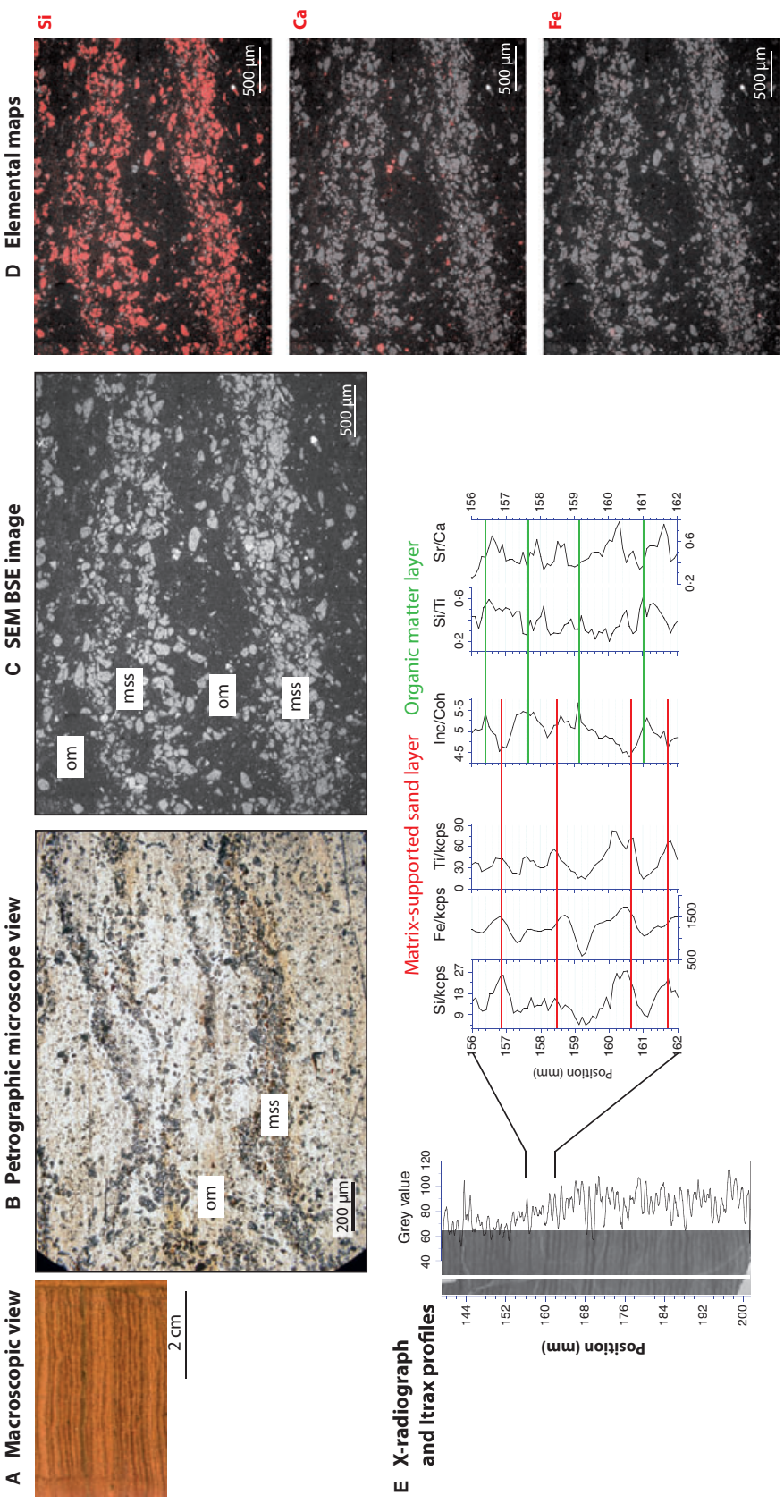

Fig. 3. Example of the Upper Laminated Facies. (A) View of the core surface. (B) Photomicrograph in plain light ('mss': matrix-supported sand lamina; 'om': organic-rich lamina). (C) SEM BSE image. (D) Elemental maps acquired using EDS. (E) Itrax measurements of selected chemical elements. From left to right: X-radiograph of a 7 cm long impregnated block used to make thin sections and its grey-scale profile along the white vertical line (denser sediments are darker); 6 mm thick close-up of selected geochemical profiles: red horizontal lines correspond to matrix-supported sand laminae and green lines correspond to organic-rich laminae. Depths are relative to the reference position of the sample in the instrument.

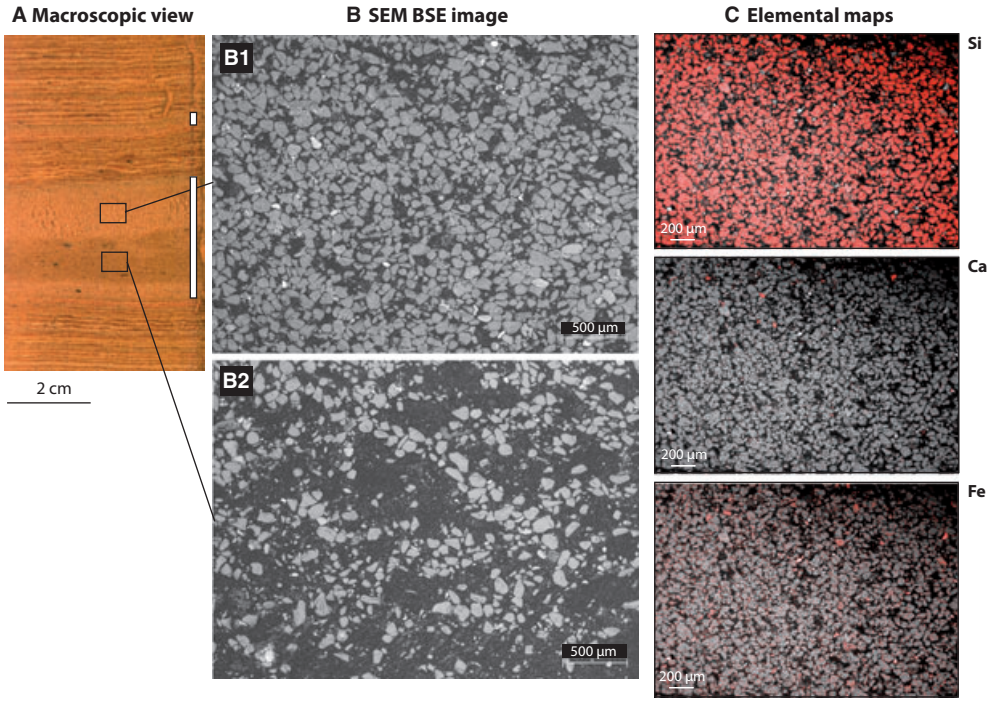

Fig. 4. Example of the Detrital Facies. (A) View of the core surface with the thickest detrital layer of the studied Lake Yoa record, at 35 cm core depth in unit VI (two detrital layers outlined by white vertical lines), embedded within Upper Laminated Facies. Note the conformable contact at the base of the detrital layers. (B) SEM BSE images of a grain to matrix-supported facies (B1) and a matrix-supported facies (B2). (C) Elemental maps acquired using EDS of a grain to matrix-supported facies; similar responses are obtained on a matrix-supported facies.

made up of organic matter. Under SEM, it is a dark and structureless lamina. In the X-radiographs, this organic-rich lamina is less dense than the two other laminae, and high in Inc/Coh and Sr/Ca, fairly high in Si/Ti and low in Si/kcps, Ti/kcps and Fe/kcps (Fig. 2E). Diatoms were visible in some cases, but in two-dimensional slices under the backscattered SEM mode, these thin-walled features are difficult to observe. Nevertheless, higher Si/Ti also point to a non-trivial presence of biogenic silica (Brown *et al.*, 2007). Occasionally, an additional thin lamina of organic matter can be seen intercalated between the first (mic) and second (mss) type of lamina.

Upper Laminated Facies (Fig. 3)

This facies is only present in unit VI. Macroscopically, its laminations consist of alternating light reddish-brown and dark reddish-brown layers (Fig. 3A). Accordingly, observations under both the petrographic microscope and the SEM reveal two kinds of laminae (Fig. 3B). The light reddish-brown layer consists of a mixture of matrix-supported and rounded medium to very fine sand grains made of Si (mss), and finer material rich in both Fe and Ca in the SEM-EDS chemical maps (Fig. 3D). This indicates a mixture of finer detrital material including mineral silts and clay, organic matter and detrital carbonates. Itrax µ-XRF profiles show a more complex pattern, but the mss lamina is usually denser (low grey value) and rich in Si, Fe and Ti, while inc/coh is low (Fig 3E). The dark reddish-brown layer is an organic-rich lamina (om) that is less dense in the X-radiograph (high grey value) and has high inc/coh, commonly high Si/Ti (Fig. 3E) and K values (not

Fig. 5. Proxy records of allochthonous input over the 6100 year Lake Yoa sequence along the composite depth scale (left) and time scale (right): selected µ-XRF profiles (10-point averages), mass-specific magnetic susceptibility (χ) of detrital material, occurrences of Detrital Facies, selected grain-size fractions, organic matter content estimated by weight loss on ignition, the grain-size *W*-ratio (see *Methods* section for explanation), and X-ray diffraction data on clay mineralogy and bulk mineralogy, expressed on a semi-quantitative scale from 1 (major) to 4 (traces). K: kaolinite; I: mica/illite; S: swelling clays; Qz: quartz; Fs: feldspar; Ca: calcite; Ar: aragonite; Do: dolomite; Di: diopside; Gy: gypsum; Th: thenardite; Ha: halite; Ka: kaolinite. Roman numerals refer to the stratigraphic units I to IV, with temporal boundaries (in ka cal BP) indicated on the right.

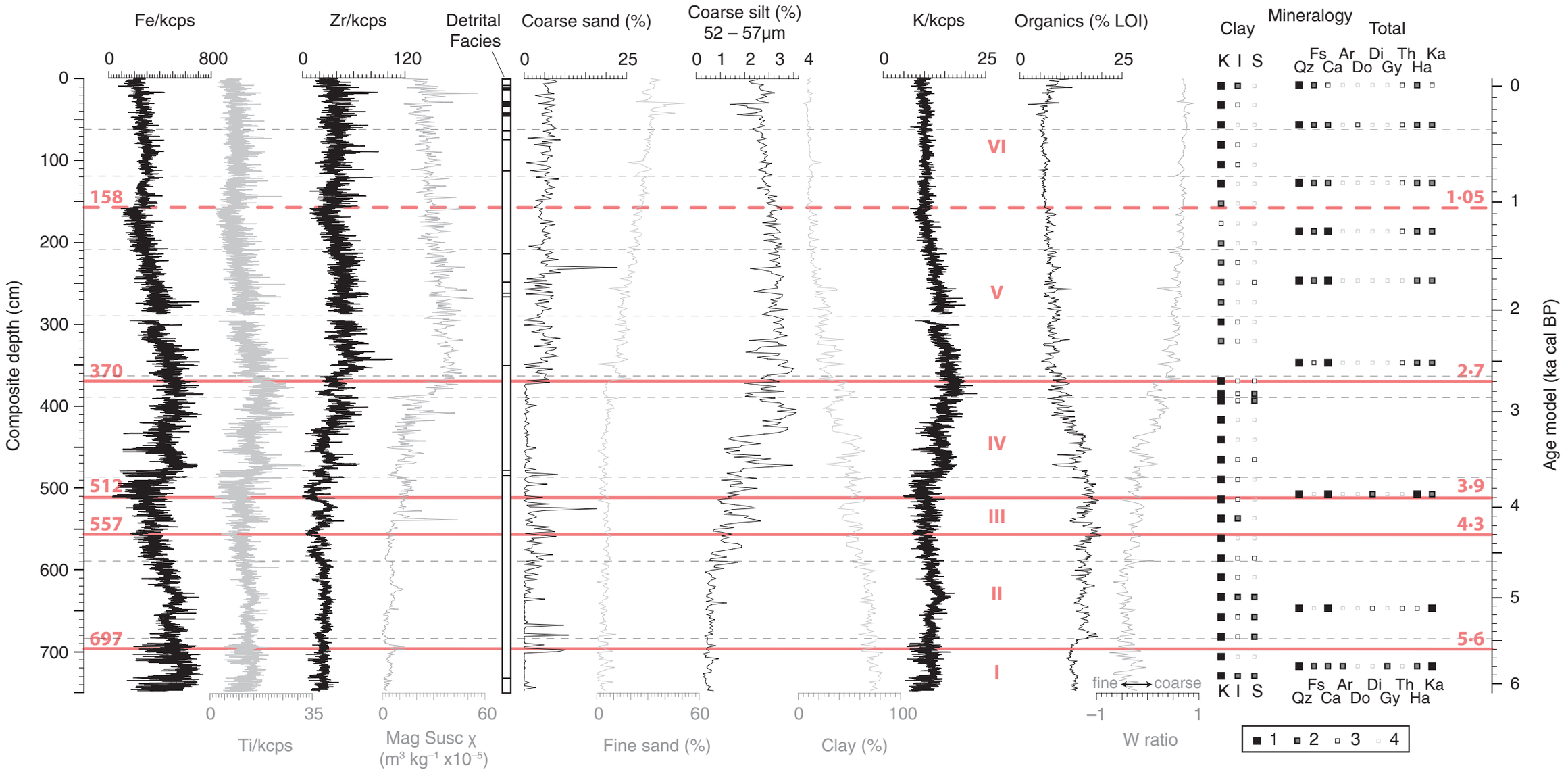
Fe/kcps
Zr/kcps
Detrital Facies
Coarse sand (%)
Coarse silt (%) 52 – 57µm
K/kcps
Organics (% LOI)
Clay
Mineralogy
Total
K I S
Fs Ar Di Th Ka
Qz Ca Do Gy Ha
Composite depth (cm)
Age model (ka cal BP)
158
370
512
557
697
1·05
2·7
3·9
4·3
5·6
VI
V
IV
III
II
I
Ti/kcps
Mag Susc χ (m³ kg⁻¹ x10⁻⁵)
Fine sand (%)
Clay (%)
fine ↔ coarse
W ratio
1 2 3 4

shown), while Sr/Ca is low (Fig. 3E). Diatoms were not visible in the thin sections; however, this does not imply their total absence because of their cryptic nature as mentioned above.

Detrital Facies (Fig. 4)

Eighteen sand layers, between 0·5 cm and 3 cm thick, interrupt the fine lamination throughout the core, with increasing occurrences towards the top (Fig. 5); only three of them coincide with peaks in the coarse-sand fraction (Fig. 5). These sand layers are matrix-supported (Fig. 4 B2), well-sorted medium sand grains composed of Si in EDS maps (Fig. 4). Some layers, or parts of them (Fig. 4), are finer-grained and can be matrix to grain-supported (Fig. 4 B1) (i.e. grains are in contact with each other; Tucker, 2001), because the sand grains are intercalated with finer detrital material rich in Fe and Ca. As far as is macroscopically visible on digital images and radiographs, and microscopically on thin sections, none of these layers seems to be erosive.

Physical, mineralogical and chemical properties

Stratigraphic changes in selected sediment properties through the Lake Yoa sequence are outlined in Figs 5 and 6. For the purpose of conciseness, only the most important patterns are described here; further detail is given in the *Discussion* section.

Mass-specific magnetic susceptibility (χ; corrected for organic matter and carbonate content) is close to zero in unit I, and remains at this level in unit II (Fig. 5). Then, it increases in units III and IV to reach a maximum of 40×10^{-5} m^3 kg^{-1} at a depth of 360 cm. From there, it progressively decreases to reach values around 20×10^{-5} m^3 kg^{-1} at the top of the sequence.

Organic-matter content is stable around 13% in unit I, then increases to 16% shortly above the unit I to II boundary and remains stable at that level in units II and III. In unit IV, it decreases steadily to values around 10%, and in unit V it declines further, slowly reaching a minimum of 4% at 50 cm depth (Fig. 5). From there, it displays a slight increase towards the top of the sequence.

The percentage abundance of coarse sand is mostly negligible throughout units I to IV, except for a few isolated peaks exceeding 10% between depths of 697 cm and 660 cm, and more frequent occurrences of 3 to 6% between 640 cm and 485 cm (Fig. 5). At 370 cm depth, that is, the unit IV to V boundary, it increases abruptly to about 5% and subsequently remains stable at 5 to 7% until the top of the sequence. Fine sand percentages are also constantly low (averaging 5%) in units I to III and the bottom half of unit IV. Around 430 cm depth, and coincident with the start of the most prominent rise in χ, the fine sand fraction increases slowly and remarkably steadily through units V and VI towards the top of the sequence, reaching a peak value of 51% at 30 cm depth. The coarse silt (52 to 57 μm) fraction is very low (<0·5%) in the lowermost part of the core, then increases in several steps between 590 cm and the upper part of unit IV to values approaching 4%, before falling slowly (and being interrupted by several lows) back to *ca* 3% at the unit V to VI boundary, and *ca* 2·5% at the top. Overall, the main trend in the coarse silt fraction resembles that of χ. In contrast, the clay percentage is *ca* 75% at the base of the sequence, and progressively decreases upwards to values below 20% shortly below the top of unit V, and only 10% at the sediment surface.

The *W*-ratio points to the dominance of fine-grained clastic material below 512 cm depth (units I to III), followed in unit IV by a transition to coarser grained clastic material characteristic of units V and VI. In general, the main trend in *W*-ratio is a mixture of the main trends in fine sand and coarse silt, and further inversely proportional to the content of organic matter, although small disagreements occur.

Inductively-coupled plasma atomic emission spectrometry geochemical analyses of the sediment are reported in Table 3. SiO_2 is the main component of the sediment between 270 cm and 158 cm depth (57·9 to 72·4%), and dominates unit VI (70·0 to 93·3%). It is followed by either CaO (in carbonates) or Al_2O_3. The iron oxide content varies between 1·05 and 3·26%.

Micro-XRF results are shown in Figs 5 to 7. The Fe/kcps profile has an undulating sawtooth pattern, with a succession of three gentle and progressive decreases, followed by three sharper increases around 470 cm, 280 cm and 158 cm depth (Fig. 5). High and low-frequency fluctuations of Ti/kcps parallel those of Fe/kcps (Fig. 5) and are highly correlated ($r = 0{\cdot}86$). Zr/kcps is low and fairly stable in units I to III, but with increasing high-frequency variability in the upper part of unit II and in unit III (Fig. 5). In unit IV, both the average value and high-frequency variability in Zr/kcps increase, to reach

peak values just above the transition to unit V. Above that level, the Zr/kcps profile resembles the Fe/kcps profile (Fig. 5). The Mn/kcps profile (Fig. 6) has average values of around 25 from the base of the core to 620 cm, above which it decreases to values around 10 in units III and IV, and values around 5 in unit V falling to *ca* 3 above 200 cm depth (Fig. 6). The main trends in Mn/Fe and Mn/Ti largely resemble that of Mn/kcps (Fig. 6). Starting from an average value between 0·04 and 0·05 (but locally peaking at 0·08) in units I and II, average Mn/Fe decreases strongly in unit III, and then more gently throughout unit IV, to values between 0·01 and 0·02 in units V and VI. At the top of unit V it shows increased high-frequency variation, including drops to background values and values close to 0·03; above 158 cm it remains more or less stable through unit VI. The same features are present in the Mn/Ti profile, except that the principal drop to average values less than 1 occurs more abruptly in the lower half of unit III.

Carbonate content as estimated by LOI ranges between 2% and 24·2%, values comparable to CaO measured by ICP-AES (0·4 to 25·7%; only the upper third of the sequence). Carbonate content, Ca/kcps and Ca/Ti all display a broadly similar pattern with stable values in units I to IV, increasing values towards the top of unit V (though less so in Ca/kcps), and a pronounced and abrupt drop in unit VI (Fig. 6). The clear difference in the geochemistry of unit VI compared with the lower units is shown in Fig. 7 where Fe, K and Ti are inversely proportional to Ca in units I to V, while this inverse relation is lacking in unit VI; in fact, K is positively correlated with Ca in unit VI. Finally, average values of Sr/Ca are generally around 0·4 in units I to IV, except for a few short intervals with values approaching 0·8, and isolated peak values up to 5. At the base of unit V, Sr/Ca increases stepwise to average values of 0·6, and again at the base of unit VI to reach values between 0·6 and 1·2 in that uppermost unit.

Minerals detected by bulk-XRD in the Lake Yoa sediment sequence are halite, gypsum, thenardite, calcite, aragonite, dolomite, quartz, albite, orthoclase and diopside. Quartz is the dominant mineral, and the feldspars albite and orthoclase are also present throughout the entire sequence but in trace quantities. Peak intensities of both quartz and feldspars progressively increase in the more recent sediments (Fig. 5). Likewise, both halite and thenardite were found in all samples but in relatively small amounts, although this pattern may have been modified by secondary precipitation during transport and storage. Gypsum was found only in the lowermost sample, from 710 cm depth in unit I. Diopside is present in two samples at 640 cm (unit II) and 500 cm (the unit III to IV boundary), and tentatively also at 710 cm. Carbonates mainly appear as calcite that is present in high abundance in units I to V, and only as traces or as a minor component in unit VI. Aragonite was only found in the sample from unit I at the base of the core. Mg-bearing calcite is present at 500 cm and 640 cm, the two levels where diopside also occurs. Clay minerals present in the Lake Yoa sequence are kaolinite, illite/mica and swelling clays. Kaolinite is ubiquitous; however, its relative concentration within unit V is lower than elsewhere (Fig. 5). Swelling clay minerals are relatively common in units I and II, and the top of unit IV, but rare or lacking in other sections.

DISCUSSION

Environmental interpretation of the sedimentary facies

A prerequisite for varve formation is the presence of sufficient seasonal contrast in weather and/or lake conditions to produce seasonal variation in the composition of the sediment flux to the bottom of the lake (O'Sullivan, 1983). In this subtropical desert location, very hot summers (mean June/July/August temperature >30°C, Table 1) with (at present) negligible precipitation alternate with long, cool windy seasons when north-easterly trade winds are strongest. In the following paragraphs, the influence of this seasonality on the formation of the different microscopic laminae is discussed.

The Lower Laminated Facies (Fig. 2)

The first type of lamina of the lamination triplets which comprises each varve in the lower part of the Lake Yoa record is composed of endogenic calcite, which is interpreted to have formed during summer (June/July/August). The rhombohedral shape of these micrite grains under SEM is similar to that of endogenic calcite reported from many lakes elsewhere (Freytet & Verrecchia, 2002). The high Ca/Ti of this lamina means that the Ca is not associated with (Ti-containing) detrital input. Endogenic calcite precipitation can be triggered by two mechanisms: (i) seasonally increasing tempera-

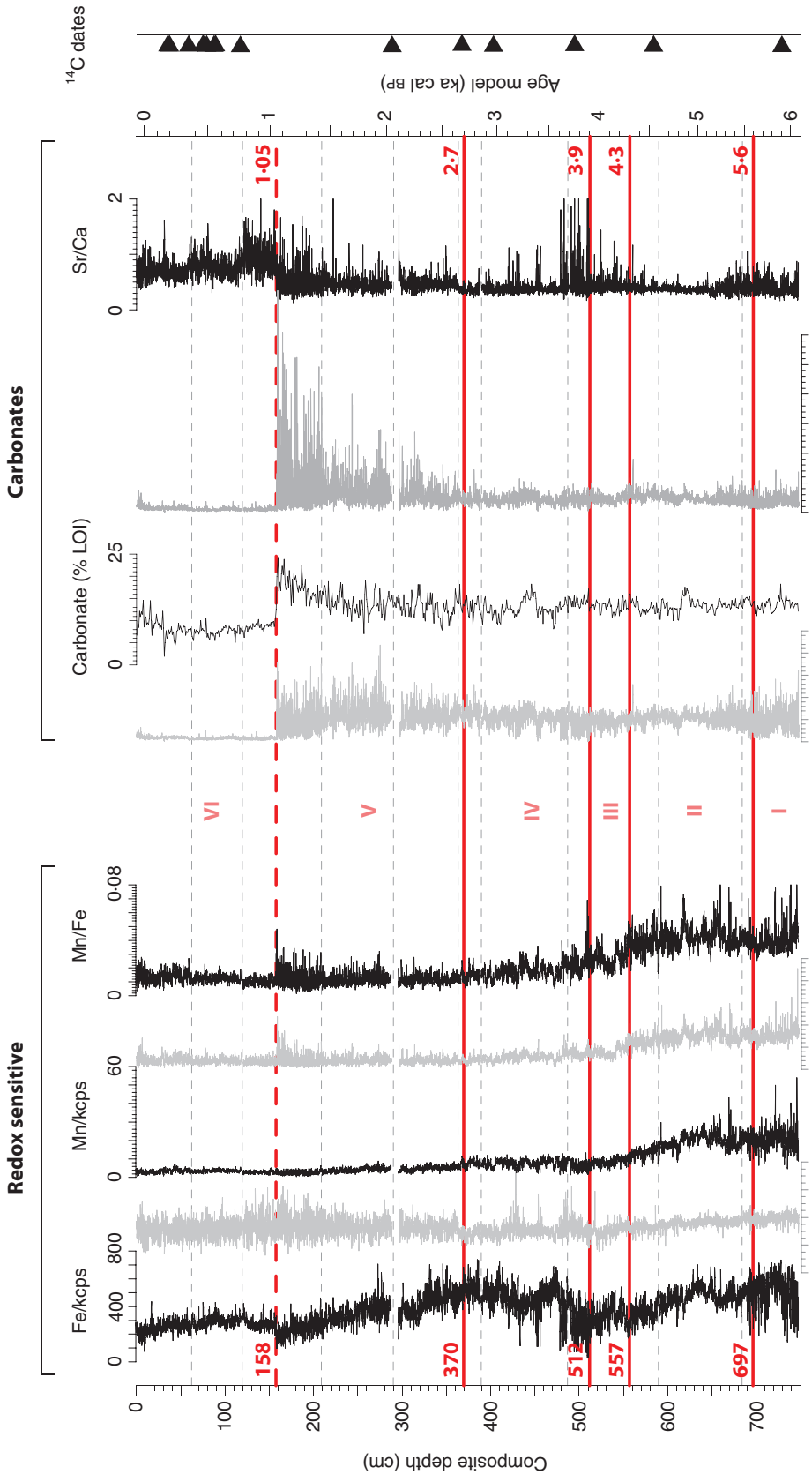

Fig. 6. Proxy records of endogenic and authigenic processes, and oxydation–reduction (redox) conditions over the 6100-year Lake Yoa sequence along the composite depth scale (left) and time scale (right): selected μ-XRF profiles (10-point averages) and carbonate content estimated by weight loss after ashing. Roman numerals refer to the stratigraphic units I to IV. Black triangles on the right vertical axis indicate the locations of 17 ^{14}C dates used to constrain the age model; see Kröpelin *et al.* (2008) for details.

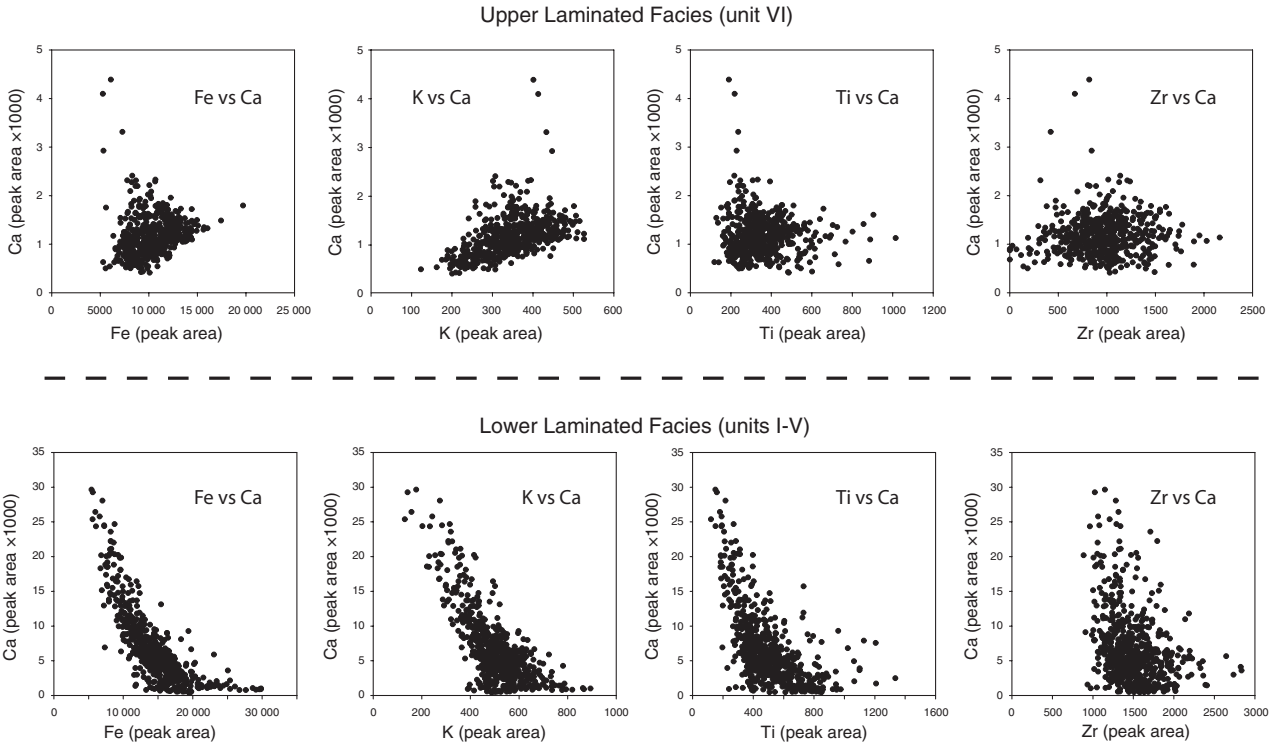

Fig. 7. μ-XRF data scatter plots of Ca versus Fe, K, Ti and Zr for one Upper Laminated Facies interval (38·8 to 44·0 cm depth) and one Lower Laminated Facies interval (251·8 to 258·5 cm depth). Analyses were obtained from two resin-impregnated blocks used to make thin sections.

ture causes over-saturation of the water column with respect to calcite; or (ii) precipitation is triggered by massive uptake of dissolved CO_2 by algal or cyanobacterial blooms (Gorham *et al.*, 1983; Dean & Megard, 1993; Lotter *et al.*, 1997). Before 3·9 ka cal BP (broadly units I to III) when Lake Yoa was fresh with significant abundances of green algae (for example, *Botryococcus, Cosmarium, Staurastrum* and *Scenedesmus*) (Kröpelin *et al.*, 2008), both processes probably contributed to endogenic calcite precipitation. However, when after 3·9 ka cal BP the freshwater phytoplankton community collapsed due to increased salinity (Kröpelin *et al.*, 2008), evaporation was probably the only process responsible for calcite precipitation in units IV and V.

The second type of lamina, which consists of rounded very fine to medium sands and finer detrital material, is interpreted as deposited during the long and windy cool season. The homogeneity and lateral continuity of the sandy laminae seen under the microscope appear to conflict with the hypothesis proposed by Kröpelin *et al.* (2008) that coarser sand was transported to the lake by saltation from nearby dunes, followed by entrapment in a soapy film at the water surface and subsequent release in the pelagic zone. Nevertheless, at least three criteria point to a directly aeolian, rather than a fluvial source. Firstly, the grain size is consistent with proximal wind-blown deposits. Short-distance aeolian sediments in the very windy environment of the present-day Sahara can contain sand grains up to 200 μm in diameter (McTainsh & Walker, 1982; Coudé-Gaussen, 1989; Goudie & Middleton, 2001) when close to potential sand sources. Secondly, the matrix-supported fabric and lack of grading is indicative of an aeolian source for its sandy component (Niessen *et al.*, 1992). Thirdly, lack of erosive contacts at the base of the sand-rich laminae and of other specific sedimentary structures argues against the presence of sub-aquatic flows such as turbidites or debris flows.

The third, organic-rich type of lamina of the lamination triplets is interpreted to result from the mixed background deposition of dead algae directly settling from the photic zone, and reworked organic and inorganic material from the littoral zone. Reworked organic material is indeed mixed with clay, as indicated by the scattered occurrence of K, an indicator of clay, across all three laminae, suggesting that this reworking is occurring all the time. The occasionally occurring second thin organic-rich

lamina intercalated between the micritic and the sandy laminae is interpreted as resulting either from the relatively sudden eradication of pelagic phytoplankton blooms at the end of the stratified season, or because a longer than usual time occurred between the seasonal end of endogenic calcite precipitation and the first sand storm. Indeed, modelling experiments of dust emission (Laurent *et al.*, 2008) suggest that the well-marked seasonal cycle of sand storms in the eastern Sahara shows strong interannual variability in terms of both intensity and timing. In short, the Lower Laminated Facies represents a background of (near-) continuous organic lacustrine sedimentation interrupted by endogenic calcite precipitation during summer, and by wind-blown detrital material mobilized during frequent sand storms in cool-season months.

Upper Laminated Facies (Fig. 3)

The Upper Laminated Facies of unit VI only contains the sandy and organic laminae. Both are similar to those of the Lower Laminated Facies, recording the two phenomena of aeolian input due to strong winds, and background sedimentation of dead algae from the epilimnion supplemented by organic material reworked from shallow areas. Re-deposition of material from peripheral, shallow areas of the lake seems to have been a dominant process since 1·05 ka cal BP, as already pointed out by Eggermont *et al.* (2008). The quasi-absence above 158 cm of micritic laminae consisting of endogenic calcite is consistent with very low aquatic productivity in the now hypersaline lake, and perhaps also influenced by cooler Late Holocene summers (Wanner *et al.*, 2008).

Detrital Facies (Fig. 4)

The fabric of the Detrital Facies is similar to that of the sandy laminae of the laminated facies: it contains well-sorted Si-rich medium sands and a mix of finer Ca and Fe-rich grains (Fig. 4). One small difference is that they are sometimes matrix-supported, and at other times they are matrix to grain-supported. The origin of this Detrital Facies remains uncertain. A range of interpretations can be ruled out: (i) deposition by turbidity flows triggered by flash floods, because this would have produced graded beds and erosional features (Mulder & Alexander, 2001); (ii) deposition of density or debris flows triggered by sub-aquatic slope failure, because this would have produced a heterogeneous sediment fabric and erosional features that are also missing here; and (iii) events of exceptional wind strength, because the size of the sand grains is identical to that of the sand-rich lamina of the laminated intervals. The relatively frequent Detrital Facies in units V and VI, deposited after establishment of the desert landscape of today 2·7 ka cal BP (Kröpelin *et al.*, 2008) and with continuous high content of coarse sand (>5%; Fig. 5), indicating the nearby presence of active dunes, most probably reflect the occurrence of exceptionally violent sand storms above or in the immediate vicinity of Lake Yoa. However, this explanation does not hold for the occasional presence of this Detrital Facies in units I to IV, when dunes in the lake basin must have been small or stabilized by vegetation. One possibility is that in the course of Mid Holocene lake-level decline, unusually prolonged dry spells would have temporarily exposed large areas of the sandy littoral zone to mobilization by wind. This interpretation is supported by a climate modelling experiment by Lézine *et al.* (2011) showing that the average duration of dry spells increased from 8·8 months at 6 ka BP, to 11 months at 4 ka BP, to 27·1 months today. Thus, prolonged dry spells were less frequent in the Mid Holocene than today, but they did occur.

Physical, mineralogical and chemical properties

Endogenic and authigenic processes

In addition to the very high resolution of μ-XRF profiles allowing the geochemical structure of the varves to be resolved, profiles for most chemical elements also show gradual trends alternating with phases of stability. The only major exception to this pattern is the sudden drop in Ca and Ca/Ti, and the parallel increase in Sr/Ca at the unit V to VI transition, dated to 1·05 ka cal BP. The combined geochemical evidence supports the microscopic observations that this change reflects the disappearance of micritic laminae composed of endogenic calcite. Iron, K, Ti and Zr are no longer inversely proportional to Ca in unit VI, as they were in units I to V (Fig. 7). As Ti and Zr are not usually incorporated into minerals taking part in endogenic or authigenic processes (Last, 2001), they are considered to be indicators of detrital input (Boyle, 2001; Croudace *et al.*, 2006). Therefore, Ca/Ti is indicative of endogenic calcite precipitation in Lake Yoa, and has moderate to high values in units I to V contrasting with consis-

tently low values in unit VI. This geochemical change is interpreted to result from the geochemical evolution of the evaporating Lake Yoa brine, as described by Gac *et al.* (1977). In their geochemical model, these authors predicted that the dilute fossil ground water springing at Lake Yoa, assuming stable ground water geochemistry through time, should evolve into a hypersaline brine depleted in Ca and Mg following their precipitation caused by continuously strong evaporation. The data presented here indicate that by 1·05 ka cal BP all dissolved Ca stored in Lake Yoa was consumed by calcite precipitation. As the lake is still fed continuously by fresh-water springs containing a significant amount of Ca, sporadic calcite precipitation occurs and is evidenced by thin but well-defined layers of endogenic calcite crystals in the upper facies. These few layers are the outliers in the scatter plots of Fe, K and Ti versus Ca (Fig. 7, upper panel). Among the minerals reported by Gac *et al.* (1977) from littoral salt crusts on the gently sloping southern shore of modern day Lake Yoa, this study confirms the presence of halite, thenardite, calcite, aragonite and dolomite in the lake sediments. In contrast, sylvite, burkeite, huntite, pirssonite, trona, nahcolite, gaylussite, magnesite and siderite were not found, all of which had been reported by Gac *et al.* (1977). The identification of thenardite (Na_2SO_4) is limited to the nine XRD samples of bulk sediment, and it has not been possible to link this mineral with a specific μ-XRF geochemical indicator. However, three samples younger than 1·05 ka cal BP still contain this mineral, implying that the Lake Yoa brine has not yet reached the threshold of Na-depletion predicted by Gac *et al.* (1977).

Redox conditions

Preservation of finely laminated sediments, such as those of Lake Yoa, indicates that no physical or biological perturbation occurs at the sediment – water interface, implying anoxic conditions in the deep parts of the basin (almost) throughout the year (O'Sullivan, 1983). These anoxic conditions can be maintained by stable temperature or salinity gradients, which prevent deep turbulent mixing or convection to replenish the deeper water column with oxygen that is continually consumed by bacterial decomposition of organic matter settling to the lake floor. There is no continuous measurement of the Lake Yoa water column, but measurement of temperature profiles during the cold and windy season in January 1999, December 2003 and November 2004, together with the subtropical location of the site, suggest a monomictic mixing regime today (van Bocxlaer *et al.*, 2011). However, given that high salinity (68 mS cm^{-1}) and elevated bottom temperature (17°C) reduce oxygen solubility by *ca* 60% compared with the cool hypolimnia of fresh dimictic lakes, injection of oxygen to the bottom can only be modest even when the water column is isothermal; thus, bottom conditions in Lake Yoa do not favour the establishment of a benthic fauna. Redox-sensitive elements detected by Itrax are Fe and Mn. As Mn/kcps and Mn/Ti have almost identical variations (Fig. 6), sedimentary Mn content is not influenced by detrital input and can therefore be used as a tracer of lake-bottom redox conditions (Croudace *et al.*, 2006). In anoxic (reducing) conditions, Mn is released from the sediment into the water column as Mn^{2+} ions. In contrast, variations in Fe/kcps and Fe/Ti curves are not parallel, the latter being relatively steady while variations in the former are similar to those of Ti/kcps (Fig. 5). This indicates that Fe mainly varies with the amount of detrital input, and that anoxic conditions were not strong enough to significantly mobilize Fe, which has a lower redox potential than Mn (Davison, 1993), from the sediment. This difference in redox potential between Mn and Fe implies that Mn/Fe can be used as an indicator of changes in redox conditions in the lower water column (Wersin *et al.*, 1991; Granina *et al.*, 2004). The present study (Fig. 6) reveals that the lower water column of Lake Yoa was less strongly oxygen-depleted prior to 4·3 ka cal BP when the lake was fresh (units I and II), and became more strongly anoxic during and after the fresh to saline transition (units III, IV and the lower part of unit V). In the upper part of unit V, deposited between 2 ka and 1·05 ka cal BP, a low background Mn/Fe is punctuated by higher values occurring with high frequency. These peaks can be explained by the buffering effect of high carbonate precipitation against the redox decline caused by organic decomposition, as pointed out by a positive correlation between Mn/Fe and Ca/Ti in this interval. Water-column mixing conditions remained stable after 1·05 ka cal BP, with little replenishment of deep-water oxygen despite yearly complete mixing of the hypersaline water column. This history of redox conditions may appear counter-intuitive when considering that: (i) the Mid Holocene fresh-water lake was more productive, favouring

deep-water anoxic conditions; and (ii) the Mid Holocene lake levels were higher than today (Kröpelin, 2007) due to a more humid climate, a situation which normally induces a more stable water column (Cohen, 2003). However, when Lake Yoa was hydrologically open and fresh 6 to 4 ka ago (Kröpelin *et al.*, 2008; Grenier *et al.*, 2009), high lake level and elevated aquatic productivity could not compensate for convective injection of oxygen into the lower water column during the mixing season. Later, near-permanent low-redox conditions developed because strong evaporation and reduced rainfall established density stratification and lowered oxygen solubility, favouring anoxic conditions. These factors compensated for the effects of stronger winds and lower lake level. Of all these interacting factors, only the increase of water density stratification may have been delayed by the constant input of fresh ground water.

In summary, the geochemical analyses reported here indicate that the bottom of Lake Yoa has been anoxic during most of the past 6·1 ka, which is consistent with the continuous preservation of fine lamination. However, significant high-frequency fluctuation of Mn/Fe suggests that overturning events did manage to temporarily modify near-bottom redox conditions, due to a partly wind-driven monomictic mixing regime and still relatively shallow lake depth.

Sediment source

Tracking the source of sediment is commonly performed using its mineralogy (Valero-Garcés *et al.*, 1999; Andrews *et al.*, 2010). However most of the minerals present in this 6100 year Lake Yoa sequence are found ubiquitously in the larger area around the lake, except for the diopside detected in units II and III. As this mineral is restricted to Quaternary volcanic formations of the Tibesti Mountains (Gèze *et al.*, 1959; Gourgaud & Vincent, 2004), its occurrence supports the idea that at least ephemeral streams were flowing into Lake Yoa during its fresh water phase (units I and II), and as late as the fresh to saline transition 4·2 to 3·9 ka cal BP (unit III). This finding corroborates the suggestion by Kröpelin *et al.* (2008) of Tibesti River inflow until as late as 3000 years ago, based on the presence of *Erica Arborea* pollen, a shrub restricted to high mountain elevations (Lézine, 2009). It also supports the palaeohydrographical network reconstructed by Grenier *et al.* (2009) for 6000 years ago, linking the Tibesti Mountain range with Lake Yoa despite a lack of direct geomorphological evidence in the modern landscape.

The mass-specific magnetic susceptibility (χ) of lake sediments is usually proportional to the concentration of magnetic minerals incorporated in allochthonous detrital material (Thompson *et al.*, 1975; Dearing, 1999). Kröpelin *et al.* (2008) interpreted trends of χ in the Lake Yoa sequence as a proxy for the input of wind-blown dust. This is confirmed here by the overall agreement between the main trends in χ and the concentration of coarse silt (Fig. 5: grain-size fraction 52 to 57 μm), showing that the magnetic signal is linked with this dust grain size, in accordance with Sun & Liu (2000). Furthermore, there is broad agreement between χ and Zr/kcps (Fig. 5), which confirms the link with detrital material because Zr usually concentrates in minerals that are resistant to chemical alteration (Haug *et al.*, 2003). Even their short-term fluctuations are frequently synchronous (for example, at 18 cm, 470 cm and 539 cm depth in Fig. 5). Notably, the principal long-term trends of magnetic susceptibility at Lake Yoa seem unaffected by the documented change in lake-bottom redox conditions, given that anoxic conditions may cause the dissolution of magnetite (Nowaczyk *et al.*, 2007). In fact, more oxic conditions occurred when χ is minimal at the base of the record, whereas more anoxic conditions prevailed when it is high later on. Another indicator of aeolian input is the grain size of the sand fraction. Following the general model that stronger winds can mobilize coarser sand grains (Bagnold, 1941; Summerfield, 1997), the occurrence of coarse sand in the core indicates stronger transporting winds than occurrences of fine sand. The concentration of fine sand seems to reflect 'background' aeolian input mobilized by north-east trade winds from sand dunes immediately north-east of the lake (Fig 1C), which increased in size and proximity throughout the last *ca* 3 ka (from the top of unit IV; Kröpelin *et al.*, 2008). In contrast, coarse sand should indicate strong sand storms, mobilizing coarser grains from these dunes.

The above-mentioned aeolian proxies (coarse and fine sand, coarse silt 52 to 57 μm, Zr/kcps, χ) all show a general rising trend throughout the Late Holocene; however, they do not match each other in detail. For instance, coarse silt rises gradually from 4·7 ka cal BP until *ca* 2·7 ka cal BP, whereas χ rises gradually from 4·6 ka cal BP but increases more sharply after 3·2 ka cal BP

until 2·7 ka cal BP, then both start a gradually declining trend towards the present. In contrast, the amount of fine sand gently rises after 2·7 ka cal BP, and coarse sand increases rather abruptly at *ca* 2·7 ka cal BP. This reflects the different response of these proxies to the same change in palaeoenvironmental conditions, possibly due to a different source area or different mechanism of mobilization. As outlined above, the steady increase of fine sand after 2·7 ka cal BP could reflect the approaching of sand dunes developing at the foot of the escarpment immediately north-east of the lake, whereas the overall constant input of coarse sand indicates that the intensity/frequency of storms did not generally increase during the last 2·7 ka. Whereas most sand is likely to be mobilized from sand dunes within the lake basin, the source of the coarse silt containing Zr and magnetic minerals has not been identified in detail. Obviously, this material must also originate from a source upwind (north-east) of Lake Yoa, although at a larger distance than the sand. It is suggested that the subtle start of silty dust deposition after 4·7 ka cal BP represents the gradual loss of vegetation cover on the greater Erdi plateau north-east of the lake. The steady decline in coarse silt and χ after reaching their maximum 2·7 ka cal BP was interpreted by Kröpelin *et al.* (2008) to reflect the eventual depletion of easily mobilized dust in this source area following the loss of all vegetation, such that dust input after that time solely represents the background rate of new bedrock erosion. This hypothesis is supported here, except that the declining trend after 2·7 ka cal BP itself is at least partly caused by the dilution effect of increasing fine sand content over the same period (Fig. 5).

Another potential cause for the start of sand sedimentation and decreased input of coarse silt after 2·7 ka cal BP could be a change in main wind direction. A systematic parallel decrease of coarse silt and magnetic susceptibility was, however, not seen between 5 ka and 3·5 ka cal BP when sporadic input of coarse sand occurred, hence ruling out this possibility. Instead, it is proposed that the aeolian proxies react to the gradual loss of vegetation cover in the larger surrounding region from around 4·7 ka cal BP, followed by growth of dunes at the foot of the nearby escarpment from around 3·0 ka cal BP.

Clay content continuously decreases throughout the Lake Yoa sequence, indicating that clay input towards the lake gradually diminished during the Late Holocene. The different depth distribution of kaolinite and swelling clay minerals (Fig. 5) shows that they are independent of each other, pointing to different sources and/or ways of transport. Whereas kaolinite is present throughout the core with only a slight reduction in unit V, swelling clay minerals suddenly decrease after 5·0 ka cal BP, with a subsequent weak maximum between 2·9 ka and 2·6 ka cal BP. Although found in dust samples from the northern and central Sahara (Goudie & Middleton, 2001), kaolinite is known to originate mainly from old and deeply weathered tropical soils found in the Sahel and the southern Sahara today, and is thus a tracer for aeolian dust originating from that region (Caquineau *et al.*, 1998) or even further south. In contrast, swelling clay minerals such as smectite do not point to a distinct source area in present-day aeolian dust (Caquineau *et al.*, 1998). This is due to the fact that they ubiquitously occur in (palaeo) topsoils throughout the Sahara (Dixon & Weed, 1995), and are thus found in dust samples from all potential source regions (Goudie & Middleton, 2001; Blanco *et al.*, 2003; Chudnovsky *et al.*, 2009). Alternatively, swelling clay minerals can also derive from mafic volcanites, such as those that occur in the Tibesti Mountains (Gourgaud & Vincent, 2004). However, the data presented here do not indicate a clear relation between swelling clays and diopside, an indicator of Tibesti provenance. Consequently, their presence in Lake Yoa sediments could either result from former fluvial input from the Tibesti, or fluvial and/or aeolian input from palaeosols formed in the Central Sahara during the humid Early Holocene. The abrupt decrease of swelling clay minerals after 5·0 ka cal BP thus either indicates the termination of fluvial input from the Tibesti, and/or early aeolian depletion of the source of these minerals in the surrounding landscape.

Statistically integrating the different grain-size indicators, the *W*-ratio reflects the generally gradual trend from predominantly fine material in the lowermost part of the core (units I and II, 6·1 to 4·7 ka cal BP) to an increasingly greater contribution of coarse material in the upper part. Its course closely follows the trend of summer (June/July/August) solar insolation at 20°N (Fig. 8); however, the connection between them is evidently indirect. The coarsening of the mineral fraction is the composite effect of increasing aeolian input relative to fluvial input resulting from the gradual loss of soil-protecting vegetation in the sur-

rounding landscape, and the build-up of coarse-grained aeolian sources in the immediate proximity of the lake.

Salinity

Despite several complicating factors (Ito & Forester, 2009), Sr/Ca has frequently been used as a rough indicator of lake water salinity (Eugster & Jones, 1979). According to the salinity reconstructions inferred from assemblages of fossil chironomids, other aquatic invertebrates, diatoms and other algae, Lake Yoa experienced a progressive increase of salinity marked by four major ecological phases in the last 6100 years (Eggermont *et al.*, 2008; Kröpelin *et al.*, 2008). Relating the geochemical data presented here to these phases, the relatively rapid transition from fresh to saline conditions dated to between 4·2 ka and 3·9 ka cal BP is accompanied by a series of increasingly high peaks of Sr/Ca in unit III and the base of unit IV. Other thresholds defined by the tolerance limits of key biota are also marked by geochemical changes: the transition to a true saline lake ecosystem (>25 mS/cm), which occurred around 3·4 ka cal BP (Eggermont *et al.*, 2008), is marked by a slight increase in Ca and carbonate values, and the 45 mS/cm threshold at the beginning of unit V (2·7 ka cal BP), by a slight but distinct increase in average Sr/Ca values. The chironomid-inferred transition towards modern salinity values of >60 mS/cm around 1·5 ka cal BP is not recorded in any of the geochemical indicators utilized in this study. The marked rise in Sr/Ca after 1·05 ka cal BP cannot be interpreted in terms of salinity change, because it simply results from the complete depletion of Ca by several millennia of enhanced calcite precipitation. All things considered, the available geochemical indicators fail to accurately show the long-term salinity evolution of Lake Yoa, despite its change from a dilute fresh-water habitat to a hypersaline brine.

The environmental history of Lake Yoa inferred from sedimentology (Fig. 8)

From 6·1 to 5·6 ka cal BP (unit I), clay content is highest and rich in swelling clay minerals, and magnetic susceptibility (corrected χ) is close to zero (Fig. 8). Both indicators point to a relatively humid climate and a vegetated tropical savannah landscape (Kröpelin *et al.*, 2008) stabilizing regional soils. Background values of 1 to 5% fine sand can be attributed to surface runoff and/or fluviatile input (Kröpelin *et al.*, 2008). Preservation of fine lamination combined with relatively high Mn/Fe values indicates a mostly anoxic or at least hypoxic deeper water column, only episodically oxygenated despite likely yearly mixing (monomixis). Any oxygen replenishing the available deep-water oxygen was obviously rapidly consumed by a high abundance of decaying algae, preventing the establishment of a benthic fauna, which would disrupt the laminations. This conceptual model of a seasonally stratified and productive fresh-water lake is supported by the variable Ca/kcps values, representing well-expressed laminae of endogenic calcite. These were probably triggered by blooms of a diverse community of green algae (Chlorophyceae) during the stratified season and the diatom *Aulacoseira* during the mixing season (Kröpelin *et al.*, 2008). This is also implied by the peak content of biogenic silica in this unit (Fig. 8).

The boundary between units I and II at 5·6 ka cal BP is marked by the first signs of regional aridification, revealed here by a first reduction in swelling clay minerals and the first occurrence of coarse sand peaks (Fig. 8). The lower part of unit II (up to 4·6 ka cal BP) is characterized by a maximum in aquatic productivity from non-diatom phytoplankton (Kröpelin *et al.*, 2008), a stable high content of organic matter (Fig. 8) and improved ventilation of the lower water column (Fig. 8: high Mn/Fe). Although still inadequate to notably increase oxygen levels, this enhanced lake mixing favoured primary productivity by regenerating nutrients from the lower water column to the epilimnion. The upper part of unit II, deposited after 4·6 ka cal BP, is characterized by: the beginning of less efficient ventilation (Fig. 8: lowering Mn/Fe); more arid conditions, as seen in the reduction of swelling clay minerals; and the first signs of soil mobilization due to loss of vegetation cover, seen in the incipient input of wind-blown dust (Fig. 8: magnetic susceptibility and Fig. 5: coarse silt fraction).

In unit III, deposited between 4·3 ka and 3·9 ka cal BP and coinciding largely with the period when Lake Yoa evolved from fresh to saline (Fig. 8), deep-water ventilation becomes drastically reduced (mean Mn/Fe values drop from 4 to 5 to below 3), and aeolian input starts rising well above its Mid Holocene background value (Fig. 8: magnetic susceptibility). By that time, the open grass savannah of the Mid Holocene had been replaced by a Sahel-type vegetation

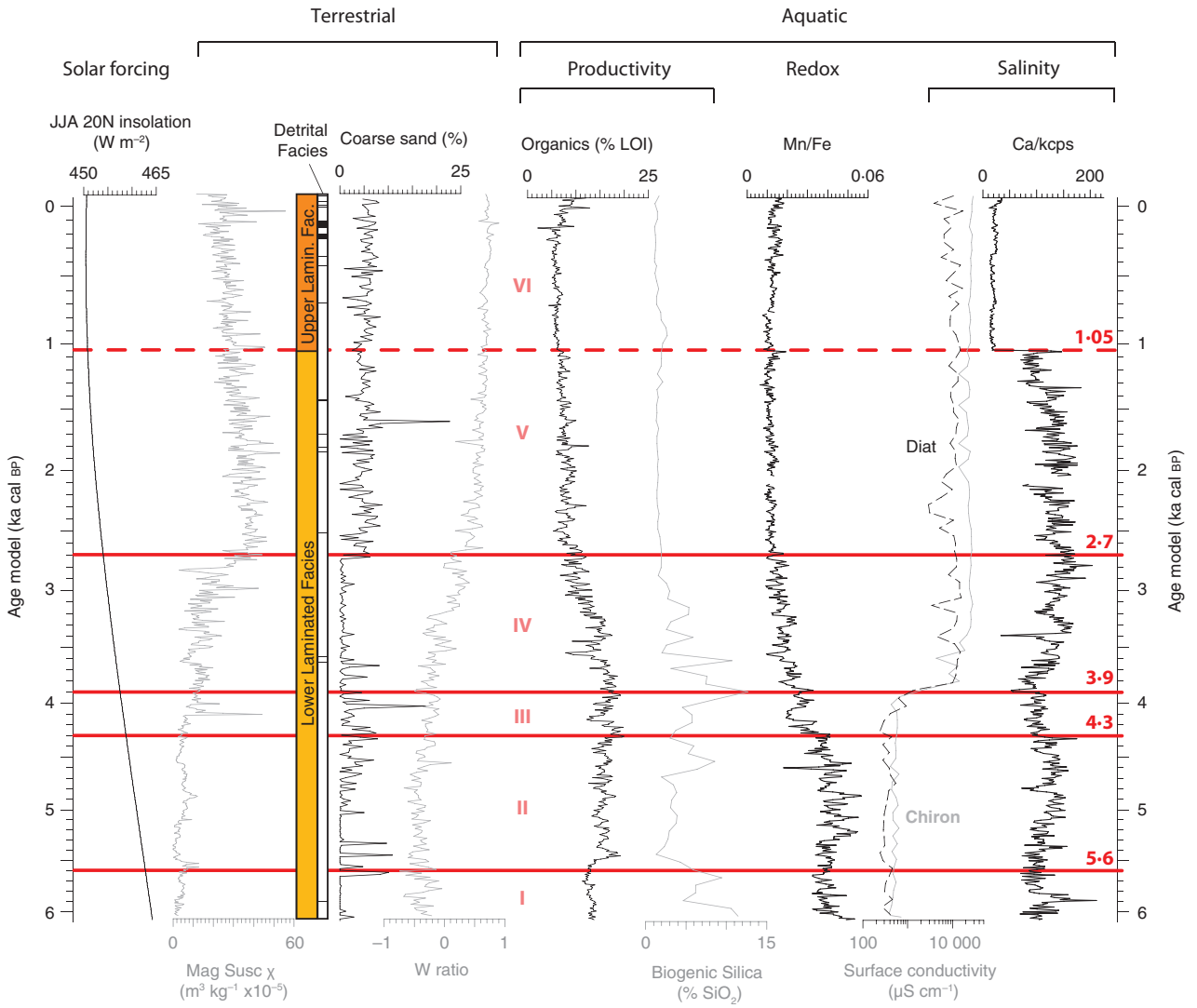

Fig. 8. Solar insolation at 20°N for June, July and August and main proxies used to infer the environmental history of Lake Yoa. Terrestrial proxies are mass-specific magnetic susceptibility (χ) of detrital material, boundaries of Upper and Lower Laminated Facies, occurrences of Detrital Facies, relative abundance of coarse sand and the grain-size *W*-ratio. Aquatic proxies are: organic matter content estimated by weight loss on ignition and biogenic silica (from Kröpelin *et al.*, 2008), Mn/Fe measured with the Itrax (1 cm averages), salinity inferred from chironomids and diatoms (from Kröpelin *et al.*, 2008), and Ca/kcps measured with the Itrax (1 cm averages). Roman numerals refer to the stratigraphic units I to IV, with temporal boundaries (in ka cal BP) indicated on the right.

and is now progressively desertifying (Kröpelin *et al.*, 2008).

At the base of unit IV deposited from 3·9 ka cal BP onwards, completion of the fresh to saline transition (Fig. 8: surface conductivity) is marked by peak values of Sr/Ca and a further reduction in deep-water ventilation (Fig. 8: drop in Mn/Fe). Following this, unit IV traces the prolonged downward slide of aquatic productivity (Fig. 8: organics) while fine-grained aeolian input continues to slowly increase, as seen in the coarse silt fraction, Zr/kcps (Fig. 5) the *W*-ratio and χ (Fig. 8). Magnetic susceptibility suggests that wind-blown dust input accelerates after *ca* 3·2 ka cal BP, but this is not mirrored in the other aeolian indicators. However, it does coincide with the incipient rise in fine sand content (Fig. 5), reflecting increasing average wind speeds and/or the start of nearby dune formation. The coarse sand fraction remained low (Fig. 8).

At the onset of unit V (2·7 to 1·05 ka cal BP), coarse silt (Fig. 5) as well as χ (Fig. 8) reach maximum values, fine sand starts its steady increase towards the present, and the fraction of coarse sand suddenly reaches modern values (Fig. 8). Following Kröpelin *et al.* (2008), these

features are interpreted as evidence for the establishment of the modern-day desert landscape with scarce vegetation cover, strong north-easterly winds blowing nearly year round, and soils becoming devoid of their mobile silt-sized fraction. Accordingly, aeolian mobilization of materials in the close vicinity of the lake increases, hence the dunes progressively migrate towards Lake Yoa from the north-east.

Starting at 1·05 ka cal BP (unit VI), the geochemistry of the lake changes completely: the brine became depleted in Ca, and calcite no longer precipitated from the water column. This change, although dramatic in the sedimentary sequence, is not due to direct external forcing, as corroborated by the fact that no aquatic biological proxies change at this boundary. Also, maximum Mn/Fe values remain lower during unit VI than during unit V. This can be interpreted to reflect less effective oxygenation of the water column, possibly because the pycnocline of the increasingly saline lake is too strong to allow complete mixing. Grain-size indicators either remain identical to the previous interval, or continue their trends (Fig. 8).

General discussion

The detailed observations of sedimentary facies under the petrographic microscope and SEM, supported by high-resolution geochemical mapping showing high-frequency variations, confirm that the laminations in the sediments of Lake Yoa are varves: a regular cycle can be observed in both the lower and the upper facies, and each type of lamina can be linked to a season. This observation confirms the annual character of the laminations based on laminae counting and absolute dating methods, that is, ^{137}Cs and ^{14}C. This study also confirms the main finding of Kröpelin *et al.* (2008) of a progressive change in the landscape surrounding Lake Yoa from a relatively humid tropical savannah 6 ka ago to a hyper-arid desert today. Indeed, almost all the sedimentological, geochemical and grain-size indicators display modest changes. One exception is carbonate that shows an abrupt jump related to the crossing of a threshold in the course of slow brine evolution, but not linked to external environmental changes in the area. The results presented here also agree with the modelling studies of Liu *et al.* (2007), showing a gradual decrease in precipitation over the Sahara during the Holocene. Furthermore, some other previous findings are supported directly by this study, such as an increase in reworked material from the littoral zone in the upper part of the core (Kröpelin *et al.*, 2008), the possible existence of at least seasonal stream inflow from the Tibesti Mountains (Kröpelin *et al.*, 2008; Lézine *et al.*, 2011) and the exhaustion of clays in soils from the surrounding landscape (Kröpelin *et al.*, 2008).

Furthermore, detrital minerals carrying Zr and magnetic susceptibility are found in the aeolian coarse silt fraction, mobilized after 4·7 ka due to landscape desiccation and thus loss of vegetation cover. There is also the possibility of increasing dry spells during the last millennium. However, several questions remain in this complex lake system: (i) it is not known whether swelling clay minerals were brought by ephemeral rivers from the Tibesti Mountains or by aeolian input; (ii) there is no explanation yet why the vegetation of neighbouring dunes was obviously disturbed between 5 ka and 3·5 ka, allowing the occasional input of coarse sand into the lake; and (iii) it is not clear why this input of coarse sand was not paralleled by input of fine sand. Without an on-site monitoring effort, including sediment trapping on the lake shores and in the water column, along with monitoring of climate and limnological parameters, the direct relation of sand content with drought or wind strength will remain qualitative.

Despite the lack of quantitative estimates of both total aeolian input and wind strength, the sedimentary and geochemical record presented here shows that Lake Yoa dried progressively during the last 6100 years, and that aeolian input was more important in the last 2·7 ka, compared with the first 3·3 ka. The increase in the *W*-ratio and the parallel decrease in organic content in parallel with solar insolation at 20°N (Fig. 8), show that the changes in the lake system itself, as well as environmental changes in the surrounding area, are controlled primarily by large-scale processes.

Additionally, it was possible to refine the sedimentological context in which the biological indicators used to reconstruct the past aquatic and terrestrial ecosystem have been preserved. In this regard, the main result is the progressive shift of Lake Yoa from a monomictic lake with relatively frequent turnover periods allowing occasional deep-water oxygenation to a more permanently anoxic water body because of the progressive salinity increase counteracting the effects of stronger wind regime and reduced lake depth. Moreover, some previously raised ques-

tions about the influence of redox conditions on magnetic susceptibility were answered, and the dramatic geochemical change that occurred at 1·05 ka cal BP was explained by natural brine evolution due to evaporation. Finally, the high quality of this sedimentary record has been established, ruling out the possibility of hiatus or erosion, hence strengthening this and previous palaeoenvironmental reconstructions.

CONCLUSIONS

The internal sedimentary structure of the laminated sediments of Lake Yoa and their geochemical structure resolved by high-resolution microfluorescence (μ-XRF) measurements allow for the understanding and the documentation of the annual cyclicity of these laminations. Varve composition can be associated with seasonal sedimentary processes: light laminae rich in endogenic carbonate were deposited during summer; laminae containing more fine and coarse-rounded sand were deposited during the windy cool season; and organic-rich laminae with fine clastic and organic reworked material from the littoral zone represent year-round background sedimentation. Calcite laminae did not form after 1·05 ka cal BP because evaporation exhausted calcium from the brine. The lower water column of the lake became gradually anoxic because of the progressive development of a pycnocline. The gradual decrease of clay content over the entire core and changes in clay composition indicate the progressive exhaustion of clays formed in Early Holocene soils of the surrounding landscape, as well as the transition from a humid towards a hyperarid landscape. There is also a simultaneous and steady increase of indicators of aeolian input, reacting to the progressive loss of vegetation cover and thus to increasing material availability. The grain-size *W*-index varies in parallel with solar insolation at 20°N. All of the sedimentological and geochemical indicators record a progressive drying of the terrestrial environment of the eastern Central Sahara during the last 6100 years.

ACKNOWLEDGEMENTS

This work was supported by the Deutsche Forschungsgemeinschaft through Sonderforschungsbereich 389 (ACACIA), the Research Foundation of Flanders (FWO-Vlaanderen, Belgium), the Centre National de la Recherche Scientifique (France), the Natural Sciences and Engineering Research Council of Canada (NSERC) and the Leibniz Society (project ECONS). Fieldwork would not have been possible without the steady backing of the Centre National d'Appui à la Recherche (CNAR), N'Djaména, Chad, through its director Baba Mallaye. The meteorological data from Faya Largeau are courtesy of the Direction des Ressources en Eau et de la Météorologie, N'Djamena, Chad. The authors thank Jean-François Crémer for geochemical analyses and their early interpretation, Christine Cocquyt for providing insight about the diatom assemblages, Charles Gobeil and André Tessier for discussions about the geochemical data, Tom Johnson and Steve Colman for assistance with exploratory grain-size analysis, Christophe Grenier for discussion about lake-level fluctuations, Bernd Ullrich and Roland Oberhänsli for providing access to XRD facilities and Mathias Vuille for help with NCEP reanalysis data. The manuscript benefited from the constructive comments of two anonymous referees and Daniel Ariztegui.

REFERENCES

Andrews, J.T., **Jennings, A.E.**, **Coleman, G.C.** and **Eberl, D.D.** (2010) Holocene variations in mineral and grain-size composition along the East Greenland glaciated margin (*ca* 67°–70°N): local versus long-distance sediment transport. *Quatern. Sci. Rev.*, **29**, 2619–2632.

Appleby, P.G. (2001) Chronostratigraphic techniques in recent sediments. In: *Tracking Environmental Changes Using Lake Sediments: Basin Analysis, Coring and Chronological Techniques* (Eds W.M. Last and J.P. Smol), pp. 171–203. Developments in Paleoenvironmental Research Series, 1, Kluwer Academic Publishers, Dordrecht, The Netherlands.

Bagnold, R.A. (1941) *The Physics of Blown Sand and Desert Dunes*. Methuen & Co., London, 265 pp.

Bengtsson, L. and **Enell, M.** (1986) Chemical analysis. In: *Handbook of Holocene Palaeoecology and Palaeohydrology* (Ed. B.E. Berglund), pp. 423–451. John Wiley & Sons Ldt., Chichester.

Blanco, A., **Tomasi, F.D.**, **Filippo, E.**, **Manno, D.**, **Perrone, M.R.**, **Serra, R.**, **Tafuro, A.M.** and **Tepore, A.** (2003) Characterization of African dust over southern Italy. *Atmos. Chem. Phys.*, **3**, 4633–4670.

van Bocxlaer, B., **Verschuren, D.**, **Schettler, G.** and **Kröpelin, S.** (2011) Modern and early Holocene mollusc fauna of the Ounianga lakes (northern Chad): implications for the palaeohydrology of the central Sahara. *J. Quatern. Sci.*, **26**, 433–447.

Boyle, J.F. (2001) Inorganic geochemical methods in paleolimnology. In: *Tracking Environmental Change Using Lake Sediments: Physical and Geochemical Methods* (Eds W.M. Last and J. Smol), pp. 83–141. Developments in

Paleoenvironmental Research Series, 2, Kluwer Academic Publishers, Doordrecht, The Netherlands.

Brown, E.T., **Johnson, T.C.**, **Scholz, C.A.**, **Cohen, A.S.** and **King, J.W.** (2007) Abrupt change in tropical African climate linked to the bipolar seesaw over the past 55,000 years. *Geophys. Res. Lett.*, **34**, 1–5.

Capot-Rey, R. (1961) *Borkou et Ounianga, Étude de géographie régionale*. Université d'Alger, Institut de recherches sahariennes, mémoire n°5, Alger, 182 pp.

Caquineau, S., **Gaudichet, A.**, **Gomes, L.**, **Magonthier, M.C.** and **Chatenet, B.** (1998) Saharan dust: clay ratio as a relevant tracer to assess the origin of soil-derived aerosols. *Geophys. Res. Lett.*, **25**, 983–986.

Chudnovsky, A., **Ben-Dor, E.**, **Kostinski, A.B.** and **Koren, I.** (2009) Mineral content analysis of atmospheric dust using hyperspectral information from space. *Geophys. Res. Lett.*, **36**, L15811.

Cohen, A.S. (2003) *Paleolimnology: The History and Evolution of Lake Systems*. Oxford University Press, New-York, 500 pp.

Conley, D.J. and **Schelske, C.L.** (2001) Biogenic silica. In: *Tracking Environmental Change Using Lake Sediments: Volume 3, Terrestrial, Algal, and Siliceous Indicators* (Eds J.P. Smol, H.J.B. Birks and W.M. Last), pp. 281–293. Kluwer Academic Press, Dordrecht, the Netherlands.

Coudé-Gaussen, G. (1989) Local, proximal and distal Saharan dusts: characterization and contributions the sedimentation. In: *Paleoclimatology and Paleometeorology: Modern and Past: Modern and Past Patterns of Global Atmospheric Transport* (Ed. M. Leinen), pp. 339–358. NATO ASI Series, Series C282, Kluwer, Dordrect, the Netherlands.

Croudace, I.W., **Rindby, A.** and **Rothwell, R.G.** (2006) ITRAX: description and evaluation of a new multi-function X-ray core scanner. In: *New Techniques in Sediment Core Analysis* (Ed. R.G. Rothwell), *Geol. Soc. Lond. Spec. Publ.*, **267**, pp. 51–63.

Davison, W. (1993) Iron and manganese in lakes. *Earth-Sci. Rev.*, **34**, 119–163.

Dean, W.E. and **Megard, R.O.** (1993) Environment of deposition of CaCO3 in Elk Lake, Minnesota. In: *Elk Lake, Minnesota: Evidence for Rapid Climate Change in the North-Central United States* (Eds J.P. Bradbury and W.E. Dean), pp. 97–114. Special paper 276, Geological Society of America, Boulder, CO.

Dearing, J.A. (1999) Holocene environmental change from magnetic proxies in lake sediments. In: *Quaternary Climates, Environments and Magnetism* (Eds B.A. Maher and T. Thompson), pp. 231–278. Cambridge University Press, Cambridge.

Dixon, J.B. and **Weed, S.B.** (1995) *Minerals in Soil Environments*, 1244 pp. Soil Science Society of America, Madison, WI.

Donner, R. (2007) *Advanced methods for analyzing and modelling multivariate paleoclimatic time series*. PhD thesis, University of Potsdam, Potsdam.

Eggermont, H., **Verschuren, D.**, **Fagot, M.**, **Rumes, B.**, **Van Bocxlaer, B.** and **Kröpelin, S.** (2008) Aquatic community response in a groundwater-fed desert lake to Holocene desiccation of the Sahara. *Quatern. Sci. Rev.*, **27**, 2411–2425.

Eugster, H.P. and **Jones, B.F.** (1979) Behavior of major solutes during closed-basin brine evolution. *Am. J. Sci.*, **279**, 609–631.

Evans, M. E. and **Heller, F.** (2003) *Environmental Magnetism: Principles and Applications of Enviromagnetics*. Academic Press, Amsterdam.

Francus, P. and **Asikainen, C.A.** (2001) Sub-sampling unconsolidated sediments: a solution for the preparation of undistrubed thin-sections from clay-rich sediments. *J. Paleolimnol.*, **26**, 323–326.

Freytet, P. and **Verrecchia, E.P.** (2002) Lacustrine and palustrine carbonate petrography: an overview. *J. Paleolimnol.*, **27**, 221–237.

Gac, J.Y., **Droubi, A.**, **Fritz, B.** and **Tardy, Y.** (1977) Geochemical behaviour of silica and magnesium during the evaporation of waters in Chad. *Chem. Geol.*, **19**, 215–228.

Gèze, B., **Hudeley, H.**, **Vincent, P.** and **Wacrenier, P.** (1959) Les volcans du Tibesti (Sahara du Tchad). *B. Volcanol.*, **22**, 135–172.

Gorham, E., **Dean, W.E.** and **Sanger, J.E.** (1983) The chemical composition of lakes in the north-central United States. *Limnol. Oceanogr.*, **28**, 287–301.

Goudie, A.S. and **Middleton, N.J.** (2001) Saharan dust storms: nature and consequences. *Earth-Sci. Rev.*, **56**, 179–204.

Gourgaud, A. and **Vincent, P.M.** (2004) Petrology of two continental alkaline intraplate series at Emi Koussi volcano, Tibesti, Chad. *J. Volcanol. Geoth. Res.*, **129**, 261–290.

Granina, L., **Müller, B.** and **Wehrli, B.** (2004) Origin and dynamics of Fe and Mn sedimentary layers in Lake Baikal. *Chem. Geol.*, **205**, 55–72.

Grenier, C., **Paillou, P.** and **Maugis, P.** (2009) Assessment of Holocene surface hydrological connections for the Ounianga lake catchment zone (Chad). *C. R. Geosci.*, **341**, 770–782.

Haug, G.H., **Günther, D.**, **Peterson, L.C.**, **Sigman, D.M.**, **Hughen, K.A.** and **Aeschlimann, B.** (2003) Climate and the collapse of Maya civilization. *Science*, **299**, 1731–1735.

Hoelzmann, P., **Gasse, F.**, **Dupont, L.M.**, **Salzmann, U.**, **Staubwasser, M.**, **Leuschner, D.C.** and **Sirocko, F.** (2004) Palaeoenvironmental changes in the arid and sub arid belt (Sahara-Sahel-Arabian Peninsula) from 150 kyr to present. In: *Past Climate Variability through Europe and Africa* (Eds R.W. Battarbee, F. Gasse and C.E. Stickley), pp. 219–256. Developments in Paleoenvironmental Research, 6, Springer, Netherlands.

International Atomic Energy Agency (2007). *Nubian Sandstone Aquifer System (NSAS) Report RAF/8/036*. International Atomic Energy Agency, Vienna, 43 pp.

Ito, E. and **Forester, R.** (2009) Changes in continental ostracode shell chemistry; uncertainty of cause. *Hydrobiologia*, **620**, 1–15.

Jackson J.A. (Ed.), (1997) *Glossary of Geology*. American Geological Institute, Alexandria, Virginia, 769 pp.

Konert, M. and **Vandenberghe, J.** (1997) Comparison of laser grain size analysis with pipette and sieve analysis: a solution for the underestimation of the clay fraction. *Sedimentology*, **44**, 523–535.

Kröpelin, S. (2007) High-resolution climate archives in the Sahara (Ounianga, Chad). In: *Atlas Cultural and Environmental Change in Arid Africa* (Eds O. Bubenzer, A. Bolten and F. Darius), 21, pp. 56–57. Heinrich-Barth-Institut, Köln, Cologne.

Kröpelin, S., **Verschuren, D.**, **Lézine, A.M.**, **Eggermont, H.**, **Cocquyt, C.**, **Francus, P.**, **Cazet, J.P.**, **Fagot, M.**, **Rumes, B.**, **Russell, J.M.**, **Darius, F.**, **Conley, D.J.**, **Schuster, M.**, **Von Suchodoletz, H.** and **Engstrom, D.R.** (2008) Climate-driven ecosystem succession in the Sahara: the past 6000 years. *Science*, **320**, 765–768.

Lamoureux, S.F. (1994) Embedding unfrozen lake sediments for thin section preparation. *J. Paleolimnol.*, **10**, 141–146.

Last, W.M. (2001) Mineralogical analysis of lake sediments. In: *Tracking Environmental Change Using Lake Sediments* (Eds W.M. Last and J. Smol), 2, pp. 143–187. Kluwer Academic Publishers, Doordrecht, The Netherlands.

Laurent, B., **Marticorena, B.**, **Bergametti, G.**, **Léon, J.F.** and **Mahowald, N.M.** (2008) Modelling mineral dust emissions from the Sahara desert using new surface properties and soil database. *J. Geophys. Res.*, **113**, D14218.

Lézine, A.-M. (2009) Timing of vegetation changes at the end of the Holocene Humid Period in desert areas at the northern edge of the Atlantic and Indian monsoon systems. *C. R. Geosci.*, **341**, 750–759.

Lézine, A.-M., **Zheng, W.**, **Braconnot, P.** and **Krinner, G.** (2011) A late Holocene pollen and climate record from Lake Yoa, northern Chad. *Clim. Past Discus.*, **7**, 2413–2444.

Liu, Z., **Wang, Y.**, **Gallimore, R.**, **Gasse, F.**, **Johnson, T.**, **deMenocal, P.**, **Adkins, J.**, **Notaro, M.**, **Prentice, I.C.**, **Kutzbach, J.**, **Jacob, R.**, **Behling, P.**, **Wang, L.** and **Ong, E.** (2007) Simulating the transient evolution and abrupt change of Northern Africa atmosphere-ocean-terrestrial ecosystem in the Holocene. *Quatern. Sci. Rev.*, **26**, 1818–1837.

Lotter, A., **Sturm, M.**, **Teranes, J.** and **Wehrli, B.** (1997) Varve formation since 1885 and high-resolution varve analyses in hypertrophic Baldeggersee (Switzerland). *Aquat. Sci.*, **59**, 304–325.

McTainsh, G.H. and **Walker, P.H.** (1982) Nature and distribution of Harmattan dust. *Z. Geomorphol.*, **26**, 417–435.

deMenocal, P., **Ortiz, J.**, **Guilderson, T.**, **Adkins, J.**, **Sarnthein, M.**, **Baker, L.** and **Yarusinsky, M.** (2000) Abrupt onset and termination of the African Humid Period: rapid climate responses to gradual insolation forcing. *Quatern. Sci. Rev.*, **19**, 347–361.

Moore, D.M. and **Reynolds, R.C.** (1997) *X-Ray Diffraction and the Identification ans Analysis of Clay Minerals*. Oxford University Press, New-York, 378 pp.

Mulder, T. and **Alexander, J.** (2001) The physical character of subaqueous sedimentary density flows and their deposits. *Sedimentology*, **48**, 269–299.

Niessen, F., **Lister, G.** and **Giovanoli, F.** (1992) Dust transport and palaeoclimate during the Oldest Dryas in Central Europe — implications from varves (Lake Constance). *Clim. Dynam.*, **8**, 71–81.

Nowaczyk, N., **Melles, M.** and **Minyuk, P.** (2007) A revised age model for core PG1351 from Lake El'gygytgyn, Chukotka, based on magnetic susceptibility variations tuned to northern hemisphere insolation variations. *J. Paleolimnol.*, **37**, 65–76.

O'Sullivan, P.E. (1983) Annually-laminated lake sediments and the study of Quaternary environmental changes – a review. *Quatern. Sci. Rev.*, **1**, 245–313.

Reimer, P.J., **Baillie, M.G.L.**, **Bard, E.**, **Bayliss, A.**, **Beck, J.W.**, **Bertrand, C.J.H.**, **Blackwell, P.G.**, **Buck, C.E.**, **Burr, G.S.**, **Cutler, K.B.**, **Damon, P.E.**, **Edwards, R.L.**, **Fairbanks, R.G.**, **Friedrich, M.**, **Guilderson, T.P.**, **Hogg, A.G.**, **Hughen, K.A.**, **Kromer, B.**, **McCormac, G.**, **Manning, S.**, **Ramsey, C.B.**, **Reimer, R.W.**, **Remmele, S.**, **Southon, J.R.**, **Stuiver, M.**, **Talamo, S.**, **Taylor, F.W.**, **Van der Plicht, J.** and **Weyhenmeyer, C.E.** (2004) IntCal04 terrestrial radiocarbon age calibration, 0-26 cal kyr BP. *Radiocarbon*, **46**, 1029–1058.

Schnurrenberger, D., **Russell, J.** and **Kelts, K.** (2003) Classification of lacustrine sediments based on sedimentary components. *J. Paleolimnol.*, **29**, 141–154.

Summerfield, M.A. (1997) *Global Geomorphology. An Introduction to the Study of Landforms*. Longman Scientific and Technical, Edinburgh Gate, Harlow.

Sun, J. and **Liu, T.** (2000) Multiple origins and interpretations of the magnetic susceptibility signal in Chinese wind-blown sediments. *Earth Planet. Sci. Let.*, **180**, 287–296.

Thompson, R., **Battarbee, R.W.**, **O'Sullivan, P.E.** and **Oldfield, F.** (1975) Magnetic susceptibility of lake sediments. *Limnol. Oceanogr.*, **20**, 687–698.

Thorweihe, U. (1990) Nubian Aquifer system. In: *The Geology of Egypt* (Ed. R. Said), pp. 601–611. Balkema, Amsterdam.

Tucker, M.E. (2001) *Sedimentary Petrology, An Introduction to the Origin of Sedimentary Rocks*. Blackwell Science, Oxford, UK, 262 pp.

Valero-Garcés, B.L., **Navas, A.**, **Machín, J.** and **Walling, D.** (1999) Sediment sources and siltation in mountain reservoirs: a case study from the Central Spanish Pyrenees. *Geomorphology*, **28**, 23–41.

Vandenberghe, J., **Mommersteeg, H.** and **Edelman, D.** (1993) Lithogenesis and geomorphological processes of the Pleistocene deposits at Belvedere. *Mededelingen-Rijks Geologische Dienst*, **47**, 7–18.

Vandenberghe, J., **Zhisheng, A.**, **Nugteren, G.**, **Huayu, L.** and **Van Huissteden, K.** (1997) New absolute time scale for the Quaternary climate in the Chinese Loess region by grain-size analysis. *Geology*, **25**, 35–38.

Wanner, H., **Beer, J.**, **Bütikofer, J.**, **Crowley, T.J.**, **Cubasch, U.**, **Flückiger, J.**, **Goosse, H.**, **Grosjean, M.**, **Joos, F.**, **Kaplan, J.O.**, **Küttel, M.**, **Müller, S.A.**, **Prentice, I.C.**, **Solomina, O.**, **Stocker, T.F.**, **Tarasov, P.**, **Wagner, M.** and **Widmann, M.** (2008) Mid- to Late Holocene climate change: an overview. *Quatern. Sci. Rev.*, **27**, 1791–1828.

Washington, R., **Todd, M.C.**, **Engelstaedter, S.**, **Mbainayel, S.** and **Mitchell, F.** (2006) Dust and the low-level circulation over the Bodélé Depression, Chad: observations from BoDEx 2005. *J. Geophys. Res.*, **111**, 1–15.

Wersin, P., **Höhener, P.**, **Giovanoli, R.** and **Stumm, W.** (1991) Early diagenetic influences on iron transformations in a freshwater lake sediment. *Chem. Geol.*, **90**, 233–252.

Wright, H.E. (1967) A square-rod piston sampler for lake sediments. *J. Sediment. Petrol.*, **37**, 975–976.

Wright, H.E. (1980) Cores of soft lake sediments. *Boreas*, **9**, 107–114.

Manuscript received 2 December 2011; revision accepted 13 September 2012